This is to certify that the
thesis entitled

DESIGN AND PROCESSING OF PERSPIRABLE SKIN
THROUGH NUMERICAL ANALYSIS

presented by

BASAK OGUZ

has been accepted towards fulfillment
of the requirements for the

Master of Science degree in Mechanical Engineering

Major Professor's Signature

May 7, 2009

Date

DESIGN AND PROCESSING OF PERSPIRABLE SKIN THROUGH NUMERICAL ANALYSIS

By

BASAK OGUZ

A THESIS

Submitted to
Michigan State University
in partial fulfillment of the requirements
for the degree of

MASTER OF SCIENCE

Mechanical Engineering

2009

ABSTRACT

DESIGN AND PROCESSING OF PERSPIRABLE SKIN THROUGH NUMERICAL ANALYSIS

By

BASAK OGUZ

An autonomous and reusable self-cooling thermal protection system (TPS) was designed for externally heated surfaces such as the surface of the space shuttle. This material system, named 'Perspirable Skin,' contains cores shrink-fitted into the holes on the Reinforced Carbon-Carbon (RCC) composite skin. The cores are made of either pure ZrW_2O_8 (zirconium tungstate) or ZrW_2O_8-ZrO_2 (zirconia) Functionally Graded Material (FGM). The choice of ZrW_2O_8 is due to its highly negative coefficient of thermal expansion in a wide range of temperatures. When the temperature increases, a gap is formed between the core and the RCC skin due to the difference in thermal expansions. The compressed coolant gas onboard is passed through this gap onto the surface. The coolant gas is expected to mix with the surface air to eliminate the frictional heating. The geometry and gradient of the cores as well as the fiber arrangement for RCC skin were designed by Finite Element Analysis (FEA). Optimal core design was successfully fabricated using powder metallurgy methods. Influences of powder metallurgy steps on the final properties of ceramic powders were also investigated, both experimentally and numerically. The effects of powder mixing on the compaction capabilities of ceramic powders, as well as dimension and density variations in the green bodies after compaction are discussed.

To my Mother and in loving memory of my Father

ACKNOWLEDGEMENTS

I would like to thank my advisor Dr. Patrick Kwon for giving me the opportunity to work on the Perspirable Skin project and for his invaluable supervision throughout my tenure as a Master's student at Michigan State University. I would also like to express my gratitude towards Dr. Dahsin Liu and Dr. Seungik Baek for being on my thesis committee.

I am grateful that I had a chance to work with such knowledgeable colleagues. Your willingness to help is incomparable and very much appreciated. I would like to thank Li Sun for his constructive input and guidance throughout my entire research project. I would also like to thank Kyunghee Park for his assistance in Finite Element Analysis of powder compaction, and Shantanu Joshi for helping me with NX Modeling of the final designs.

Finally, I would like to thank my mother, Nurfer Oguz, for being such a great role model; and my fiancé, Steven Wagner, for his endless support. Without them, I would not have been able to accomplish this mission. Thank you for always being there for me.

TABLE OF CONTENTS

LIST OF TABLES

LIST OF FIGURES

(Images in this thesis are presented in color.)

CHAPTER 1

INTRODUCTION

1.1. MOTIVATION

Thermal Protection System (TPS) is an essential component of reusable aerospace vehicles like the space shuttle. It protects the vehicle from the aerodynamic heating generated at the surface, which is caused by the combination of compression and surface friction by the atmospheric gases. During the reentry into the Earth's atmosphere, the orbiter travels at speeds exceeding 27,000 km/h, and the surface temperatures can reach as high as 1650°C [1]. The friction at the surface is caused by the attempt to slow the vehicle down from such high speeds to the landing speed [2]. The maximum temperature of 1650°C is reached 20 minutes before touchdown [1].

The space shuttle orbiter is composed of numerous advanced materials, but the main structure is mostly made of 2024-T6 aluminum and graphite- epoxy [3]. Both of these materials can only endure temperatures up to 175°C; therefore, a TPS is required to prevent heat from transferring into the vehicle so that the structural frame does not go beyond this temperature limit [2, 3]. Without a TPS, the whole structure would degrade at high temperatures. Thus, it is a crucial element for the protection of the vehicle structure as well as the occupants.

The motivation of this thesis is to propose a multifunctional material system, which provides cooling for several parts of the TPS that are exposed to the highest temperatures during re-entry into the Earth's atmosphere. The proposed design, called "Perspirable Skin", is an autonomous and reusable system, which is expected to significantly reduce the surface temperature of the hottest areas caused by frictional heating.

1.2. CURRENT THERMAL PROTECTION SYSTEM (TPS)

The main task of the TPS is to protect the orbiter from excessive heating during re-entry; however, it must be designed such that it can accommodate several other conditions during flight. These conditions include extremely cold temperatures (as low as -156°C) and also local heating from several engines and motors [2, 3]. Therefore, the TPS selected for a space shuttle is composed of several different materials due to the wide variation of temperatures that the vehicle experiences. Each material's thermal properties, durability, and weight determine the extent of its application on the vehicle. The variety of temperatures and the corresponding parts of the space shuttle are shown in Figure 1. This figure is taken from a NASA contractor report from 1989 and shows the highest temperature as 1440°C [3]. However, it was later reported that the maximum temperature reached is around 1650 °C [1, 2].

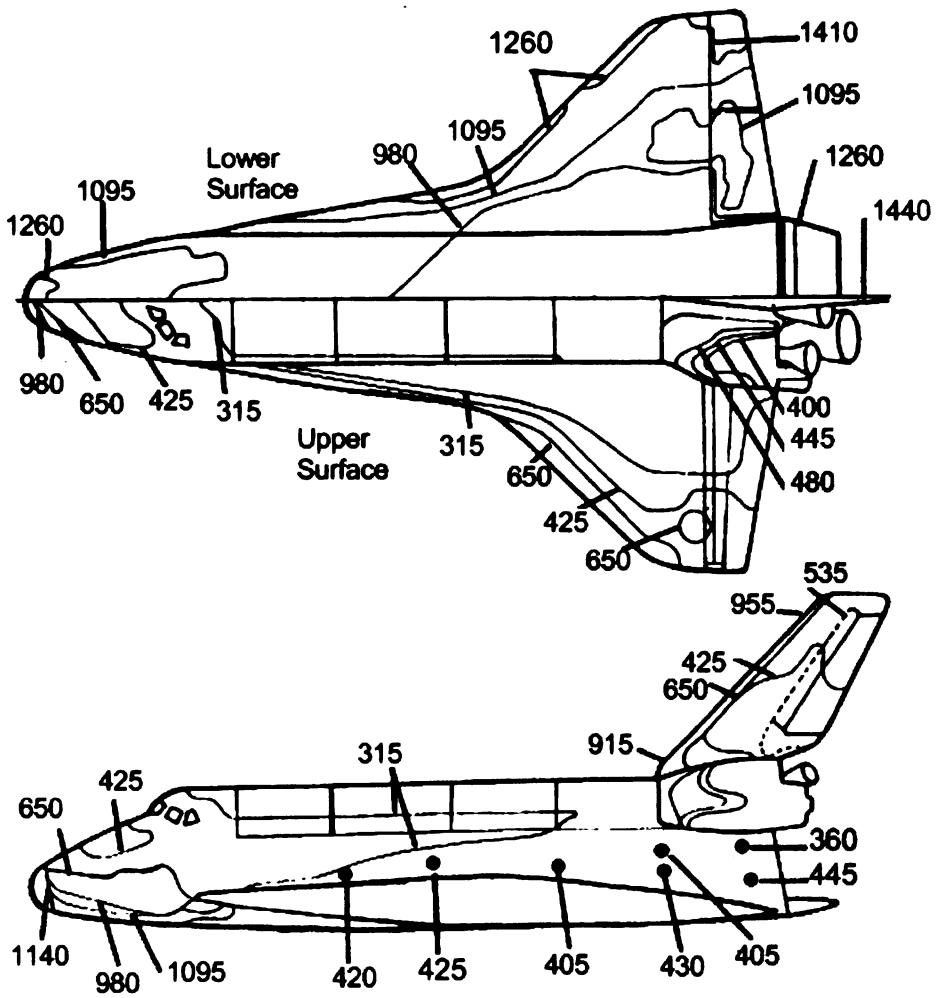

Figure 1. Maximum temperatures that different parts of the space shuttle experiences during ascent and re-entry. All temperatures shown are in degrees Celsius [3].

The original TPS is composed of four main materials. These materials include Reinforced Carbon-Carbon (RCC), low-temperature reusable surface insulation tiles (LRSI or white tiles), high-temperature reusable surface insulation tiles (HRSI), and felt reusable surface insulation (FRSI or black tiles) blankets [2, 3].

The FRSI blankets are found on the upper section of the bayload doors and the inboard sections of the wing upper surface and cover about 25 percent of the

vehicle. They protect these areas from temperatures between 175°C and 370°C. The white tiles (LRSI) cover the upper surface of the vehicle. Due to their high reflectivity, they reduce the solar heat gain from the sun. In contrast, the black tiles (HRSI) have high emissivity, which becomes crucial for heat elimination during the re-entry into the atmosphere. Black and white tiles are made of a similar material, and together they guard the vehicle from temperatures between 648°C and 1345°C. Most of the white tiles have been replaced with fibrous insulation blankets, also known as Advanced Flexible Reusable Surface Insulation (AFRSI), in order to accommodate the flight requirements more effectively [2].

The hottest areas of the orbiter during re-entry are the nose cone, the leading edge of its wings, and the area directly behind the nose cap of the lower surface, also known as the chin panel [1]. The surface temperature of the nose cone rises almost instantly when the vehicle re-enters into the atmosphere [5]. RCC, a light gray composite, along with Inconel foil insulators and quartz blankets, protect these areas from the highest expected temperatures and aerodynamic forces [4, 5]. A schematic of the orbiter TPS and the areas covered with RCC panels is shown in Figure 2.

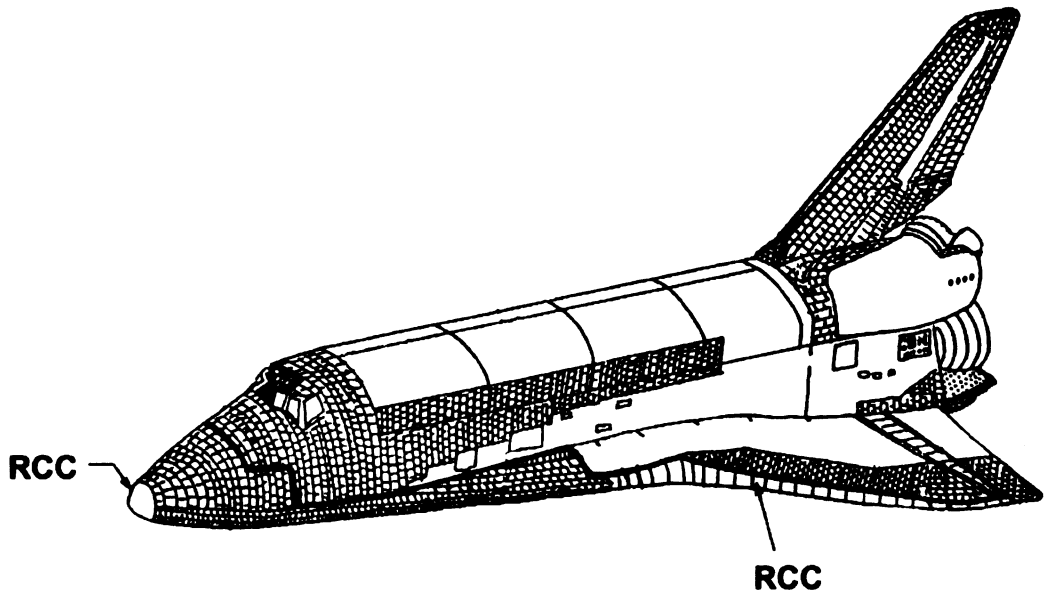

Figure 2. Schematic of the orbiter TPS [3]

The leading edges of the wings contain 22 RCC panels, which are manufactured at Lockheed-Martin's Missile and Fire Control Facilities in Dallas, Texas. These panels can withstand temperatures up to 1770°C. Even though they are able to endure very high temperatures, the RCC panels have very high thermal conductivity. For this reason, insulating blankets and tiles are needed behind the panels [6]. RCC panels must also have an oxidation protection coating such as SiC, Si_3N_4 or SiO_2 in order to resist the oxidizing environments [5]. However, when surface temperatures reach as high as 1650°C, the thermal ablation/erosion is expected to happen very rapidly. If the coating layer erodes, the whole TPS will be damaged, which would jeopardize the safety of the whole

vehicle. Therefore, a new TPS design with self-cooling capability is introduced in this study.

1.3. INTRODUCTION TO PERSPIRABLE SKIN DESIGN

The proposed design is a multifunctional material system, which is arranged in a 'Peg and Hole' fashion. The RCC skin of the space shuttle is designed to have multiple holes that contain cores (pegs). These cores would either be made of zirconium tungstate (ZrW_2O_8) or Functionally Graded Material (FGM) containing ZrW_2O_8 and zirconia (ZrO_2). The choice of ZrW_2O_8 is based on its unusual isotropic negative thermal expansion (NTE) over a wide range of temperatures (0.3-1050K) [7, 8]. In this temperature range, its Coefficient of Thermal Expansion (CTE) ranges from –6.5 to $-13.2\times10^{-6}K^{-1}$ [7]. The M-O-M transverse vibrations (where M is Zr or W in this case) in ZrW_2O_8 crystal cell causes the contraction of the M-M distance, resulting its negative thermal expansion [7].

In humans, perspiration is a part of the body's thermoregulation system. When the temperature of the skin gets higher than normal temperature, the sweat glands expand and produce a fluid consisting mainly of water and a small amount of dissolved solids. When this fluid evaporates from the skin, it will result in a cooling effect. Perspiration decreases when the temperature of the skin decreases. Perspirable Skin design discussed in this thesis works in a similar

fashion as human perspiration to regulate the surface temperature of externally heated surfaces such as the space shuttle orbiter.

When the surface temperature of Perspirable Skin increases during reentry, a gap is formed between the core and the RCC skin, mainly caused by the shrinkage of the core due to its negative thermal expansion property. Once the temperature reaches the working temperature, this gap becomes large enough to introduce coolant gas, which is onboard within the space vehicle, onto the surface. The flow of coolant gas mixed with atmospheric air is expected to significantly decrease the surface temperature at the orbiter's nose cone, chin panel, and the leading edge of the wings caused by frictional heat during the reentry.

The highest working temperature for Perspirable Skin is expected to be around 750°C, which is limited by the dissociation of ZrW_2O_8 at 777°C. However, it is expected that the Perspirable Skin will function around 700°C, the surface will be cooled, never reaching the highest surface temperature observed (1650°C) with the current TPS design. As the surface temperature decreases, the gap starts to close again. Therefore, the whole design of Perspirable Skin is an autonomous cooling system for the reentry vehicle. A simplified schematic of this concept is shown in Figure 3.

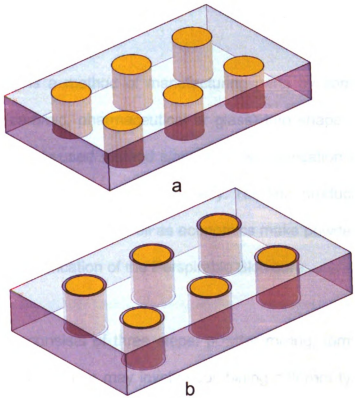

Figure 3. Basic schematic of the Perspirable Skin design (a) at room temperature (b) at maximum working temperature (750 ^{o}C)

The space vehicle has a design life of 100 missions [3]. Perspirable Skin provides a reusable and self-regulating system that meets this design criterion. The current TPS of the orbiter only provides protection from the high temperatures endured during re-entry to the atmosphere. The proposed design combines protection as well as cooling, which provides for a safer design alternative, protecting the vehicle structure and its occupants.

1.4. POWDER METALLURGY

Powder metallurgy is a method of manufacturing parts by compacting/forming powders (metal, ceramic, pharmaceutical or glass) into shape and/or sintering them. It is a commonly used method since it allows fabrication of parts of wide range of sizes with good dimensional accuracy. The final products exhibit net or near-net shape [9]. Precision, as well as economics make powder metallurgy the best method for the fabrication of the Perspirable Skin core.

Powder metallurgy consists of three steps: powder mixing, forming operations, and sintering. The initial step may involve combining different types of powders or blending powders of the same type by breaking particles or agglomerates into smaller particles through mechanical agitation. Particles may vary in size and shape; thus, this is an important step to ensure that the properties will be uniform throughout the finished part [9, 10]. During the mixing step, several additives might be added to the powder mixture, such as lubricants or binders. Lubricants improve the flow characteristics significantly, while binders help increase green strength [9].

The shaping operations involve utilizing stress to form blended powders into desired shapes. This step is performed with close dimensional control. There are numerous shaping operations, such as injection molding, extrusion, slurry techniques, freezing techniques, and compaction [11].

The most common method for pressing mixed powders into shape is the conventional cold uniaxial compaction. It involves applying pressure along one axis using hard tooling at room temperature. Generally, a die, along with an upper and a lower punch, are used to perform the operation. The pressure may be transmitted from both bottom and top punches, or in some cases the bottom punch is stationary and the pressure is transmitted from a single punch. This uniaxial compaction process is shown step-by-step in Figure 4. Samples produced after compaction are called "greens". The final density of a green sample depends on the compaction pressure and the powder characteristics [9, 11].

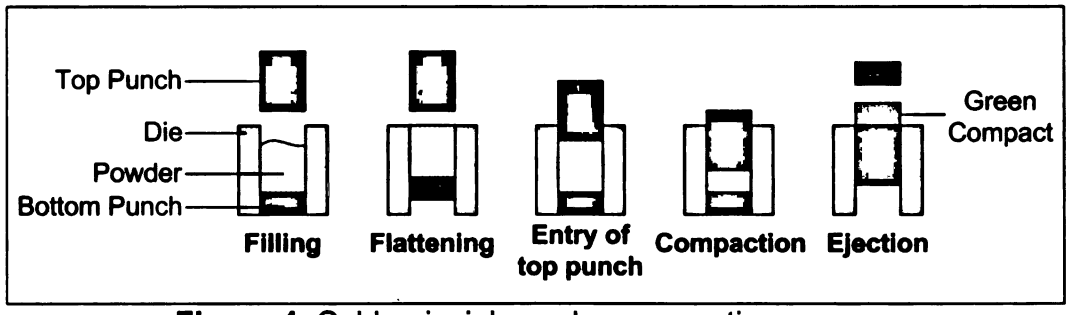

Figure 4. Cold uniaxial powder compaction process

After compaction, the green samples are not fully dense. Generally, in the case of ceramics and metals, they require additional processing, such as sintering, to obtain a denser part. Sintering is a thermal process that involves bonding of particles together at high temperatures by solid-state atomic transport phenomenon. The green compact is heated in a controlled-atmosphere furnace to the temperatures below its melting point; however, in some cases the

formation of a liquid phase might be involved. The bonding occurs due to the growth of the cohesive neck at particle contacts. After sintering, the properties observed in the green state, such as strength and density, are significantly improved [9, 11].

Subsequent to the three main steps of the powder metallurgy, occasionally some additional finishing operations might be necessary in order to obtain specific features or improve the dimensional accuracy of the final part. These operations may include machining or surface finishing. Since such additional operations would increase the manufacturing cost, it is often desired to obtain the final geometry/dimensions through the previous step(s).

As mentioned previously, powder metallurgy is the most suitable method for manufacturing the core of the Perspirable Skin. The fabrication process is discussed in detail in sections 2.3 and 2.5 of this thesis. Additionally, the effects of powder mixing in the compaction capabilities of ceramic powders, as well as variations in final dimensions and densities of green compacts are investigated in Chapter 3.

1.5. FUNCTIONALLY GRADED MATERIAL (FGM)

A functionally graded material is defined as a composite material that has gradual change in the composition and structure over its volume. Due to this gradual change, the material is non-homogeneous and the properties vary with location. This basic concept is shown in Figure 5. FGM applications are used in many fields, such as aerospace, biomedical, automotive and manufacturing [13]. The composition and properties of the FGM component depend on the specific application for which it is made.

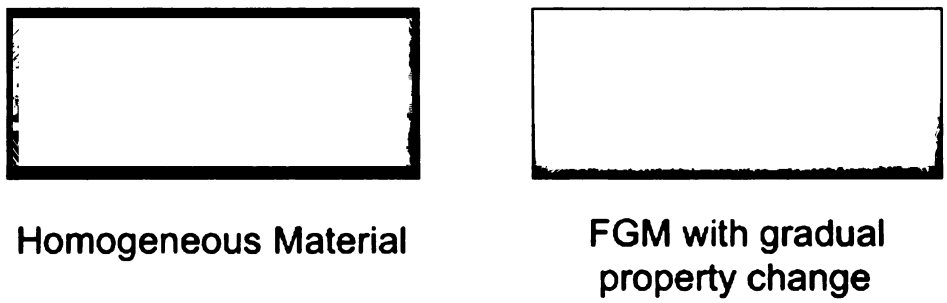

Figure 5. Basic concept of functionally graded materials

In the current study, FGM containing ZrW_2O_8 and ZrO_2 is proposed as a potential core material for the Perspirable Skin application. The important property of this kind of FGM is the continuous variation from negative to positive in the radial thermal expansion. During the reentry of the space shuttle, a temperature gradient is expected along the thickness of the TPS. While the outer surface temperatures are as high as $1650^{o}C$, the temperatures inside are expected to be around $175^{o}C$ [3]. Utilizing an FGM core that has a negative CTE

at the top surface and near-zero CTE at the bottom portion allows it to produce a large gap opening with the skin at the top surface while the bottom portion remains in contact. The FEA modeling and the fabrication of the FGM core are discussed in detail in Chapter 2.

1.6. FINITE ELEMENT METHOD (FEM)

Recently, modeling physical phenomena with the aid of computers has made it easier for engineers and scientists to be able to understand and predict complex processes. Analytical descriptions of such physical phenomena are called mathematical models, and they are described by complicated differential and integral equations. Most of the time, the geometrical domains of these equations are very challenging. Mathematical models and numerical methods, along with the help of computers made it possible for scientists and engineers to compute practical engineering problems with much less effort [14].

There are several numerical methods that are used in finding approximate solutions to partial differential equations (PDE). Some of the most common ones used for engineering applications include the Finite Element Method, Finite Difference Method (FDM), and Finite Volume Method (FVM). The development of FEM started in the mid-1950s for solving complex structural analysis problems [15]. Currently, it is the most commonly used method in structural mechanics,

whereas FVM and FDM are more widely used in solving Computational Fluid Dynamics (CFD) problems.

FEM is a powerful method because it allows for solving practical engineering problems that have complicated geometries and boundary conditions. The complex geometric domains are divided into numerous simpler subdomains called *finite elements,* which are attached together at points called *nodes*. Once the domain is divided into finite elements, algebraic equations are established for each of these elements from the governing equations of the problem. Finally, the relationships from all of the elements are collected back together in order to obtain the solution for the entire domain [14].

Currently, numerous commercially available FEM software exist that are widely used by engineers. Some of the most common ones include ANSYS (Ansys, Inc., USA) and ABAQUS (Dassault Systèmes Simulia Corp., USA), which were implemented in this study. ANSYS (Version 11.0) was the choice of software for the FEA of the Perspirable Skin design and the details are discussed in Chapter 2. For the numerical analysis of powder compaction, which is introduced in Chapter 3, ABAQUS (Version 6.6) was preferred.

1.7. MODIFIED DRUCKER-PRAGER / CAP PLASTICITY MODEL

The modified Drucker-Prager/ Cap plasticity model, which is offered in the library of the ABAQUS software, is commonly used to model frictional materials, such as granular-like soils and rocks. These types of materials exhibit pressure-dependent yield, meaning that the material becomes stronger as the pressure increases. This model can also be used for modeling the uniaxial compaction of ceramic powders since they exhibit similar behavior [15].

The modified Drucker-Prager/ Cap plasticity model is based on the addition of a cap yield surface to the original Drucker-Prager shear failure surface which was introduced by Drucker and Prager [15, 17, 18]. Therefore, the yield surface has two main segments: The pressure dependent Drucker-Prager shear failure surface and a cap yield surface that intersects the equivalent pressure axis. Between these segments, a transition section exits in order to provide a smooth surface. The main purposes of the cap are [15]:

1. It bounds the yield surface in hydrostatic compression and therefore provides an inelastic hardening mechanism to represent plastic compaction.
2. It provides a softening function of the inelastic volume increase created as the material yields on the Drucker-Prager shear failure and transition surfaces in order to control volume dilatancy as the material yields in shear.

The yield surface is shown in Figure 6. The x-axis represents the equivalent pressure, p, and the y-axis represents the square root of the second invariant of the deviatoric stress, $\sqrt{J'_2}$ [15, 16].

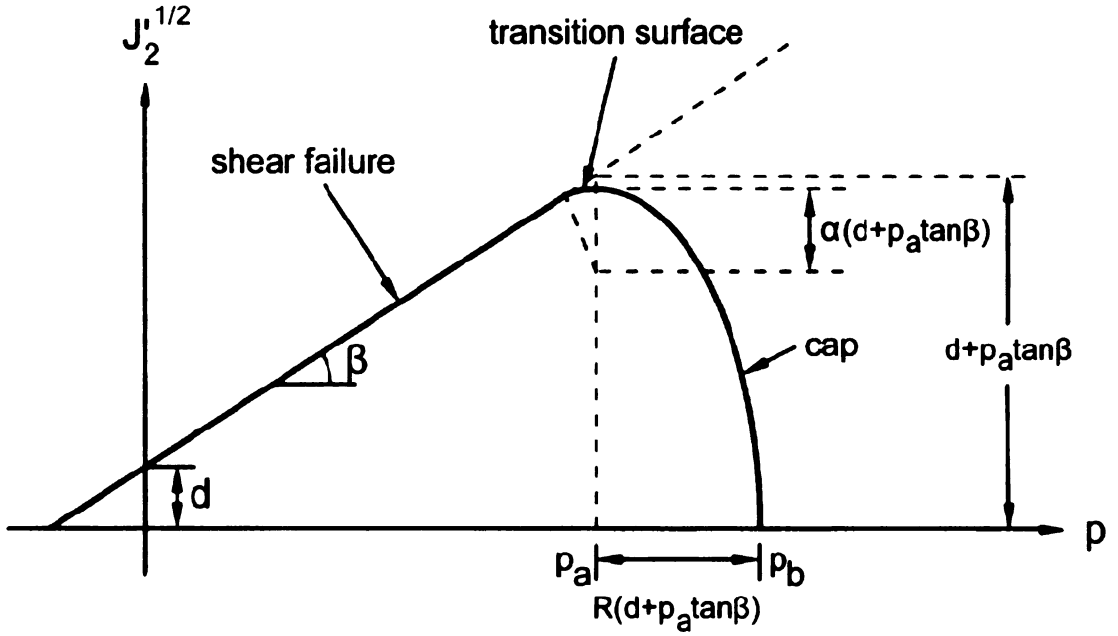

Figure 6. Modified Drucker-Prager/ Cap Plasticity Model yield surface [15]

There are several important parameters used in the formulation of the modified Drucker-Prager/ Cap plasticity model and are required as input when modeling ceramic powder compaction in ABAQUS. These parameters are also shown in Figure 6. They include unique material properties, such as the internal angle of friction (β) and the cohesion of the material (d). The transition surface parameter (α) is usually a small number between 0.01 and 0.05 and is used to provide a smooth transition between the cap and the shear failure surface. Cap eccentricity (R) is a material parameter, which controls the shape of the cap. Also shown in this Figure 6 are P_a and P_b, which represent the evolution parameter that

signifies the volumetric plastic strain driven hardening/softening and the hydrostatic compression yield stress, respectively [15, 16].

For ceramic powder compaction, the modified Drucker-Prager/ Cap plasticity model allows the effects of stress states to be addressed during several steps of the process, such as during compaction and the removal of the upper punch, and after the ejection of the green sample from the die. Since the formulation of the model satisfies the description of material responses to the environment and applied stress states, it also allows calculation of the density distributions both during the compaction and ejection processes as well as after ejection [16].

CHAPTER 2

PERSPIRABLE SKIN DESIGN

2.1. DESIGN APPROACH

The design process consisted of defining the concept, determining the best materials for the application as well as establishing the final geometry using finite element analysis (FEA), and testing the manufacturability of the final design. In order to find the ideal design for the system, several components were investigated. These components include:

1. Ideal material for the NTE core
2. Best carbon fiber arrangement for RCC skin
3. The optimal dimensions that will yield a large enough gap distance for the coolant gas to exit
4. Core geometry that will provide an efficient route for the coolant gas to be delivered to the surface
5. Alternative materials that will be most economical, while providing ease in manufacturing of the core using powder processing methods

2.2. MATERIAL SELECTION FOR THE CORE

2.2.1. Materials with Negative Thermal Expansion Property

As mentioned previously, the core for the Perspirable Skin design should have negative CTE in order to achieve a gap between the core and the RCC skin at high temperatures. Isotropic negative thermal expansion is a very uncommon property. Several NTE materials were investigated in the search for the best material for the core. Five ceramic materials with isotropic negative thermal expansion are shown in Table 1 below.

Table 1. Isotopic negative thermal expansion materials [19-25]

Material	CTE range (10^{-6} K^{-1})	Temperature range for NTE (K)
ThP_2O_7	-9.3 to 4.3	573-480
UP_2O_7	-7.1 to 3.1	773-1773
ZrV_2O_7	-11.1 to 15.4	380-875
ZrW_2O_8	-13.2 to -6.5	3-1050
HfW_2O_8	-12.9 to -6.4	3-1050

Figure 7 shows the dependence of the relative expansion of these materials on temperature. It can be seen that not all of the materials listed in Table 1 show a negative thermal expansion throughout their entire solid state. $FThP_2O_7$, UP_2O_7, and ZrV_2O_7 exhibit positive thermal expansion when temperatures are lower than their corresponding ranges listed in Table 1. Only ZrW_2O_8 and HfW_2O_8 feature negative CTE over the whole solid state. However, Hf (Hafnium) is a rarer

element than Zr (Zirconium). For this reason, ZrW_2O_8 was chosen as best core material for the Perspirable application due to its isotropic negative thermal expansion over a wide range of temperatures.

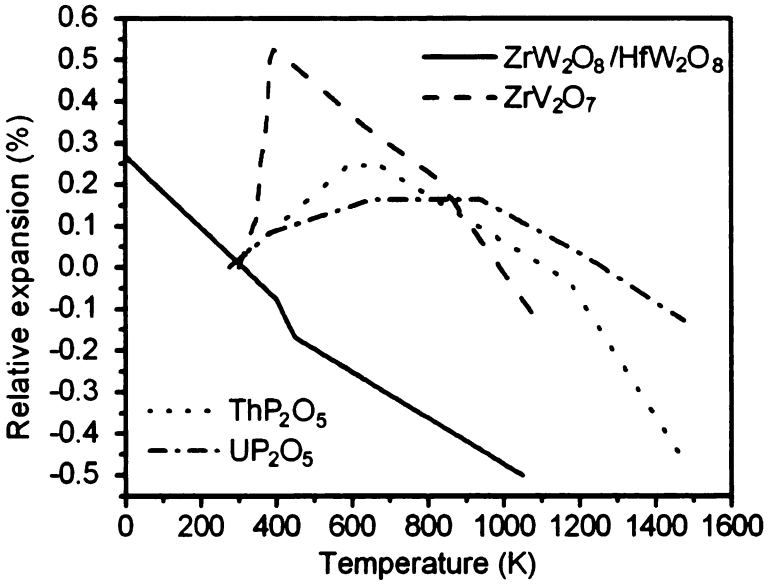

Figure 7. Temperature dependence of the relative expansion of NTE materials

2.2.2. Negative Thermal Expansion Mechanism

The basis for the isotropic negative thermal expansion of the ceramics discussed in 2.2.1 is the M-O-M linear linkage. In the case of ZrW_2O_8, the M-O-M linkage is either Zr-O-Zr or W-O-W. All of the five materials have an open, low-density framework crystal structure. Their M-O bond is very strong and the coordination of oxygen is only twofold. These characteristics have two closely related outcomes. First, the thermal expansion of the M-O bond is very low, and the thermal vibration of oxygen will is very low in the directions of the M atoms. Second, the thermal vibration of oxygen perpendicular to the M-O-M linkage

must be very high. With these unique thermal motions, as oxygen atoms vibrate, M cations are pulled together and this causes the negative thermal expansion of these materials [19, 20, 22].

A simple schematic of thermal contraction caused by thermal motion is shown in Figure 8. The solid circles represent cations and the hollow circles represent oxygens. The low temperature bond positions are shown with solid lines, and the high temperature bond positions are shown with dashed lines. The arrows indicate the direction of vibration for the oxygens [19].

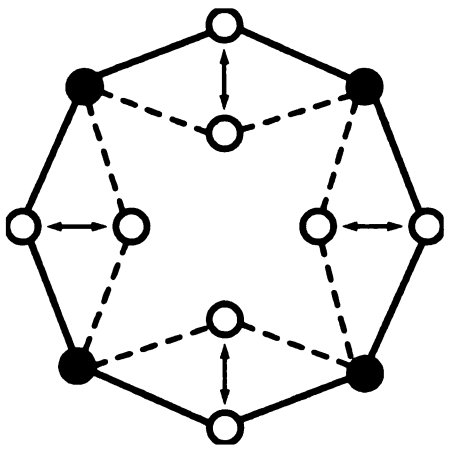

Figure 8. Schematic of thermal contraction caused by thermal motion

2.3. FABRICATION OF ZrW_2O_8

Our group has fabricated bulk ZrW_2O_8 through the in-situ reaction of WO_3 and ZrO_2 [26, 27].The two powders were mixed with the 2:1 stoichiometric ratio of WO_3 and ZrO_2 (mass ratio is m_{WO3}: m_{ZrO2} =1:0.266). ZrO_2/WO_3 mixtures with

other mass ratios result in a wide variety of ZrW_2O_8/ZrO_2 composites [28, 29]. The ramp/soak profile shown in Figure 9 was used to produce ZrW_2O_8 and the resulting microstructure is shown in Figure 10.The balanced reaction can be expressed as follows:

$$ZrO_2 + 2WO_3 \rightarrow ZrW_2O_8 \quad (1)$$

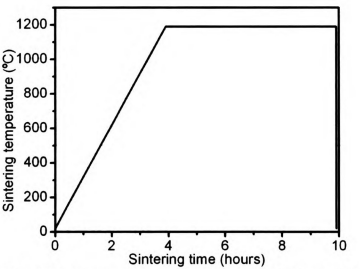

Figure 9. The ramp/soak path used for producing ZrW_2O_8

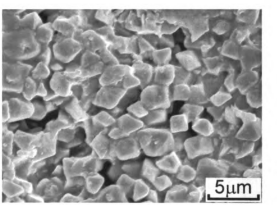

Figure 10. The microstructure of the ZrW_2O_8 substrate.

2.4. FINITE ELEMENT ANALYSIS (FEA)

2.4.1. Material Properties and Boundary Conditions

The finite element modeling was carried out using ANSYS (Version 11.0, Ansys, Inc., USA). Both the assembly conditions and working conditions were simulated. This required performing both thermal and structural analyses. The material properties required for such analyses include elastic modulus, shear modulus, Poisson's ratio, temperature dependant CTE, and thermal conductivity of each material. For modeling layered composites such as laminated RCC, ANSYS offers a layered structural solid element (SOLID46). This element allows the user to input the thickness, orientation and material properties of each layer. 3D isotropic and 3D woven orthogonal RCC, as well as the core were modeled using a different structural element (SOLID45).

The core and the RCC skin were modeled as quarter-cylinder and quarter-hollow-cylinder respectively due to the symmetric structure. The axisymmetry boundary conditions as well as several other displacement boundary conditions were applied to both parts. The corner edge (axisymmetry) of the core was fixed in the x and y directions but was free to move in the z-direction. This boundary condition allows the core to expand and shrink in every direction. Additionally, the RCC skin will apply constraining force on the core so it will not move in the z-direction freely. The RCC skin was only constrained on the outer circular edge

such that it could not move in the z-direction. This allows the skin to expand, shrink, and bend as the actual skin in flight may experience. Figure 11 shows these boundary conditions graphically.

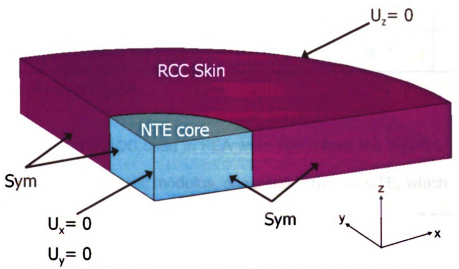

Figure 11. Boundary conditions for finite element modeling

2.4.2. Material Properties for RCC

Several different fiber arrangements were compared to find the optimized structure for RCC. These arrangements included 3-D orthogonal, 2-D fabric laminated, and isotropic. The microstructure of a 2D fabric laminate RCC composite sample (Agency for Defense Development (ADD), South Korea) is shown in Figure 12.

Table 2. Various parameters of RCC used in FEA [30]

Designation	Young's Modulus (GPa)		Shear Modulus (GPa)	CTE ($10^{-6}K^{-1}$)	
	Longitudinal	Transverse		Longitudinal	Transverse
2D Fabric Laminate	118	4.1	6	1.3	6.1
3D Woven Orthogonal	55	96	17.5	1.3	1.3
3D Isotropic	14	-	-	2E-7*	2E-7*

* Testing results by the TMA

Most properties of the RCC used in FEA were taken from the report of Sheehan et al. [30], such as the elastic modulus, shear modulus and CTE, which are listed in the Table 2. The CTE of isotropic RCC was tested from the RCC samples which were rectangular parallelepipeds with edge lengths 10.6mm, 7.0mm and 7.0mm. The value also is shown in Table 2. The temperature dependant thermal conductivity data was obtained from the report of Savage [5]. The Poisson's ratio of 0.2 was used based on the report of Tanabe et al. [29].

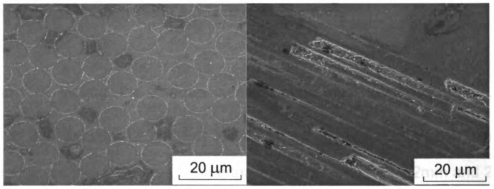

Figure 12. Microstructure of the RCC composite sample at a) fiber-cutting direction and b) fiber-parallel direction

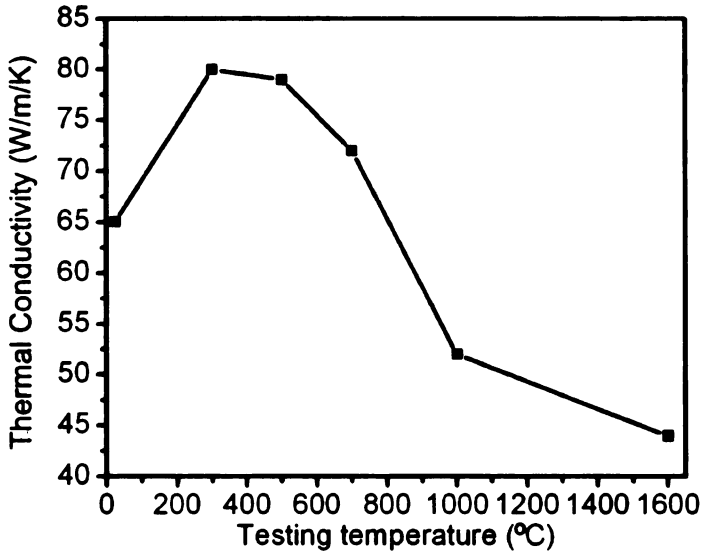

Figure 13. The temperature dependence of thermal conductivity of RCC [5]

2.4.3. Material properties for ZrW_2O_8

Most thermomechanical properties of ZrW_2O_8 were experimentally determined. The CTE and Young's modulus of the ZrW_2O_8 were measured using a Thermomechanical Analyzer (TMA: Setaram 95, France) with the heating and cooling rates of 1°C/min in the argon gas environment.

For the CTE testing, the ZrW_2O_8 samples used were cylindrical with 7.51mm diameter and 5.68mm height. For Young's modulus testing, the samples were rectangular parallelepipeds with the edge lengths of 12.6mm, 4.2mm and 2.5mm. Three samples were tested for CTE and Young's modulus. The CTE variation is less than 5% and the maximum discrepancy in the Young's modulus data is 6% in the three samples. Therefore, it was considered that the CTE and Young's

modulus testing results are consistent; and each reported value in the paper is the average of the corresponding results of three samples.

The Young's Modulus of ZrW_2O_8 was found to be 4.31 ± 0.13GPa at room temperature. The CTE-temperature relationship of the ZrW_2O_8 substrate is shown in Figure 14. As expected, the CTE of ZrW_2O_8 is negative and uniform for a wide range of temperatures before or after a sharp change around 160°C due to the **α**- to **β**- ZrW_2O_8 phase transition [22]. The CTE of the ZrW_2O_8 at room temperature is $-8.09 \pm 0.65K^{-1}$.

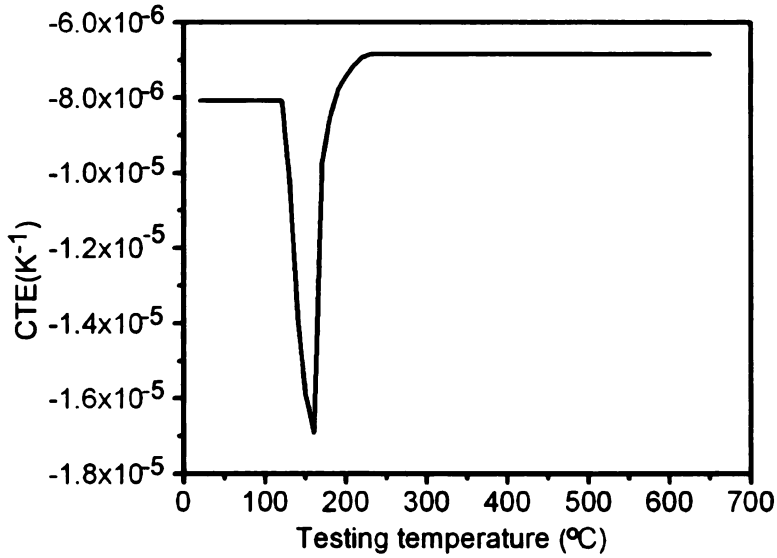

Figure 14. The temperature dependence of the CTE of ZrW_2O_8

The high temperature thermal conductivity of ZrW_2O_8 was measured using the laser flash method (FlashLine 5000, USA) from room temperature to 710°C. The results are shown in Figure 2.5 (*Test was performed by Dr. Xun Shi at Prof. Uher*

group at University of Michigan, USA). Around 160°C, a sharp peak, corresponding to the **α**-to-**β** ZrW_2O_8 phase transition can be observed. The room temperature phase is phase **α**, and its thermal conductivity is around 0.89 $Wm^{-1}K^{-1}$, a result that is very close to the reported value of 0.82 $Wm^{-1}K^{-1}$ [30]. The high temperature phase **β** features a nearly constant thermal conductivity at 0.985 $Wm^{-1}K^{-1}$ between 500 to 710°C. The results can be seen in Figure 15 and Table 3.

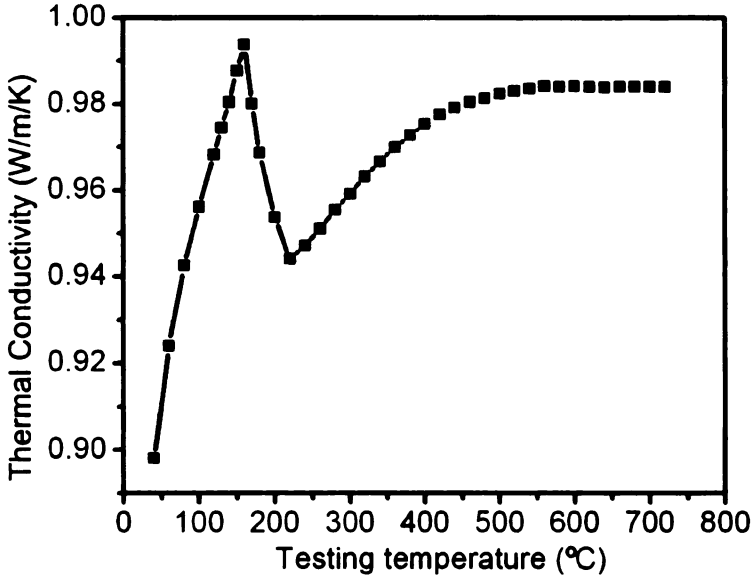

Figure 15. The temperature dependence of thermal conductivity of ZrW_2O_8

Table 3. CTE of ZrW_2O_8 at various temperatures

Temperature	25°C	100°C	150°C	>300°C
CTE ($10^{-6}K^{-1}$)	-8.09 ± 0.65	-8.56 ± 0.67	-16.5 ± 0.98	-7.3 ± 0.45

Our data indicate that the thermal conductivity of the phase β is higher than the phase α. It is known that ZrW_2O_8 exhibits a crystalline structure, and usually a crystalline material possesses a high thermal conductivity. However, our data

show the thermal conductivity of ZrW_2O_8 is very low. From the report of Mary et al. [22], the dimension of the unit cell ZrW_2O_8 is extremely large when compared with common ceramics. This structural characteristic provides more phonon vibration modes to hinder the heat flow in solid. Consequently, the thermal conductivity of ZrW_2O_8 is very low.

The Poisson's ratio was taken as 0.3 from the report of Drymiotis et al [33]. Then its shear modulus (G) was calculated using the Young's Modulus and Poisson's ratio.

$$G = \frac{E}{2(1+\nu)} \tag{2}$$

2.4.4. Flow through Annular Space formed by Two Coaxial Tubes

In order for compressed coolant gas to be successfully discharged to the surface, a large enough gap opening must be obtained between the core and the RCC skin. The minimum gap distance that makes the flow possible will also assist in determining the appropriate dimensions, such as the diameter for the cores and the holes. Assuming laminar steady flow, the velocity of the fluid flow through the annular space formed by two coaxial tubes can be expressed as function of radius using the following equation [34]:

$$u(r) = \frac{1}{4\mu}\frac{dP}{dx}\left[r^2 - a^2 - \frac{b^2 - a^2}{\ln(b/a)}\ln\left(\frac{r}{a}\right)\right] \tag{3}$$

In equation (3), r represents the radius and a and b are inner and outer radii respectively. μ is the kinematic viscosity of the coolant fluid and dP/dx is the pressure gradient. These dimensions are shown graphically in Figure 16 below. Equation (3) used to calculate radial location of maximum velocity.

$$r = \sqrt{\frac{b^2 - a^2}{2\ln(b/a)}} \tag{4}$$

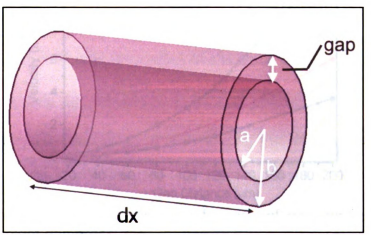

Figure 16. Several parameters used in equation (3)

Assigning a value for the outer radius and the gap distance, the inner radius can simply be obtained by subtracting the gap distance from the outer radius value. The inner and outer radii dimensions have very little effect on the velocity; rather the gap distance and the length of the tube have the most influence. Assuming the coolant fluid is nitrogen gas, the maximum fluid velocity was plotted as a function of gap distance at different pressures. The length of the tube was taken as 8mm, which is equal to the thickness of the RCC TPS [2, 35]. The relationship is shown in Figure 17. It is obvious that the fluid velocity increases as the gap

distance and the pressure of the compressed coolant gas increases. For gap distances below 60 μm, the velocity was very close to zero. Considering this, it was determined that the minimum gap distance should be at least 80 μm in order to accomplish successful discharge of the coolant gas to the surface. The dimensions of the core and the RCC skin hole were selected accordingly.

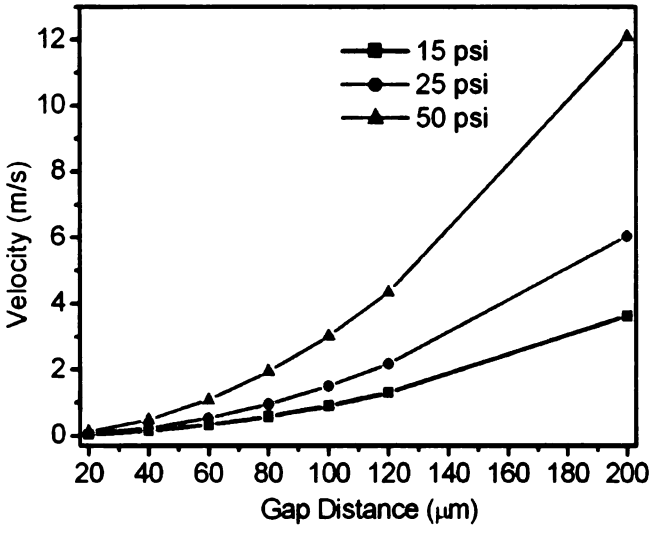

Figure 17. Maximum fluid velocity as a function of gap distance for different compressed coolant gas pressures

2.4.5. Determination of the best RCC structure

The assembly of the system is a shrink-fitting process expected to occur at a high temperature such as 750°C. When the RCC TPS and the core are isothermally heated to 750°C, the core shrinks and the hole on the RCC TPS expands creating a diametrical interference. This interference makes it possible to slide the core into the hole of the RCC skin. The assembled structure is then

cooled to room temperature. In order to achieve a secure contact between the two materials, the system should be designed such that the diameter of the hole becomes smaller than the diameter of the core at room temperature. This causes the stresses on the core a as well as skin at lower temperatures, guaranteeing a tight fit.

As mentioned previously, the gap distance opening should be 80 μm or larger in order to for the coolant gas to be released successfully to the surface. Through FEA, it was determined that the radius of the pure ZrW_2O_8 core should be at least 15mm to satisfy this requirement. Several smaller radii for the core were tested and the results were not satisfactory. For the RCC skin, a 14.98mm for the hole radius was used, which guarantees a secure fit. Any larger radius causes loss of contact between the two materials at room temperature, meaning that the ZrW_2O_8 core slides off the hole as shown in Figure 18 [36].

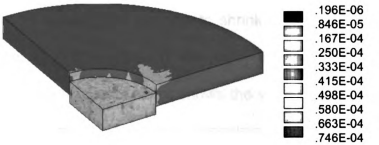

Figure 18. Von Mises stress plot showing that full contact between the ZrW_2O_8 core and the RCC skin at room temperature is lost when inner radius of RCC is higher than 14.98mm

In order to determine the best fiber arrangement for the RCC skin, four RCC structures were investigated. These structures included 3D isotropic, 3D woven orthogonal, and two 2D laminates with [0/45/-45/90]s (quasi-isotropic) and [0/90]s (cross-ply symmetric) configurations. In the evaluation of the best design, the maximum gap opening at working and assembly temperatures as well as minimum stresses at contact surfaces at room temperature were considered. In order to calculate the gap distance between the two materials caused by the shrinkage of ZrW_2O_8 core and the expansion of RCC in the assembly conditions, the temperature was increased to 750^{o}C in the FEA model for both parts. The gap distance was calculated by adding the shrinkage value of the ZrW_2O_8 core diameter to the expansion value of the RCC hole diameter. Figure 19(a) shows gap distance for the isotropic RCC modeling.

From 750^{o}C, both materials were cooled back down to room temperature. This causes the core to expand and the skin to shrink. Since the radius of the hole becomes smaller than the radius of the core, stresses are expected in the structure for a secure fit. Figure 19(b) shows the von Mises stress result for the isotropic RCC modeling. This two-step modeling process also represents the whole assembly process.

The FEA results for the other three RCC structures are similar to Figure 19. However, the gap distance and the stress values vary depending on the RCC

structures due to the variations in the thermal and mechanical properties. A comparison of the results for each RCC structure is shown in Table 4 as well as the corresponding tensile strengths [30].

Table 4. The summary of gap distance at working temperature (750°C) and the stress at room temperature (RT) between ZrW_2O_8 core and the various types of RCC skin

Designation	Gap (μm)	Stress (Mpa)	RT tensile strength (Mpa)*	
			Longitudinal	Transverse
3D Isotropic	64.41	11.7	41	5
3D Orthogonal	77.19	27.8	170	300
[0/45/-45/90]s	79.4	18.5	300-350	2.8-5.0
[0/90]s	79.4	18.8	300-350	2.8-5.0

*Data resource: [30]

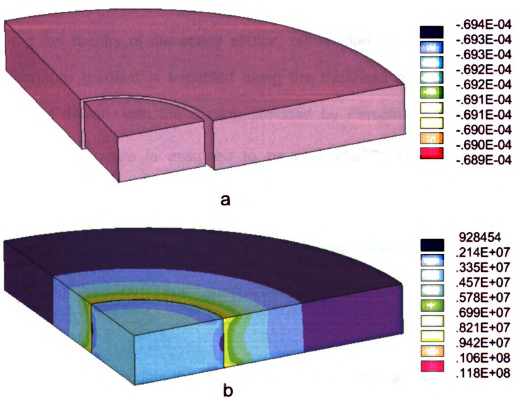

Figure 19. The FEA results for the isotropic RCC case (a) assembly temperature gap distance (b) von Mises stress at room temperature

Table 4 shows that the quasi-isotropic RCC ([0/45/-45/90]s) and cross-ply symmetric RCC ([0/90]s) resulted in the maximum gap distance of 79.4μm. However, for both cases, the maximum stress at room temperature exceeded the tensile strength in the transverse direction. This result also applies to 3D isotropic RCC, leaving the 3D woven orthogonal RCC the only fiber arrangement applicable to Perspirable Skin. Despite the slightly lower gap distance resulting from the 3D woven orthogonal RCC, its highest tensile strength in both directions provides the safest operation.

2.4.6. Design of the ZrW_2O_8 core

During the reentry of the space shuttle, rather than a uniform temperature, a temperature gradient is expected along the thickness of the TPS [3]. In the proposed design, with the cooling provided by Perspirable Skin, the highest surface temperature is assumed to be only 750^{o}C. Thus, the temperature gradient in the design was assumed to be 750^{o}C for the outer surface and 100^{o}C for the interior part. This assumption is reasonable since the interior temperature is 175^{o}C for the 1700^{o}C outer surface temperature for the RCC panels [3].

In order to accommodate the temperature gradient, the geometry of the ZrW_2O_8 core can not be a simple cylindrical shape as shown in Figure 19. It has to be changed so that it has a larger radius at the top surface and a smaller radius at

the bottom part. When this new geometry experiences this temperature gradient, the top surface of the core will shrink significantly due to the endured high temperature resulting in a large gap at the top surface, while the bottom part of the core will still maintain contact with the RCC skin because of the much lower bottom temperature. This will also avoid sliding conditions shown in Figure 18.

The first geometry considered consisted of two attached cylinders with the same height. At room temperature, the top cylinder had a radius of 15mm and the bottom one had a radius of 7.5mm. The hole radius was 14.995mm at the top and 7.49mm at the bottom. In order to model a thermal gradient throughout the material, a coupled thermal and structural analysis was performed in ANSYS. Figure 20(a) shows the temperature distribution in the structure under the new temperature gradient and Figure 20(b) shows the gap opening.

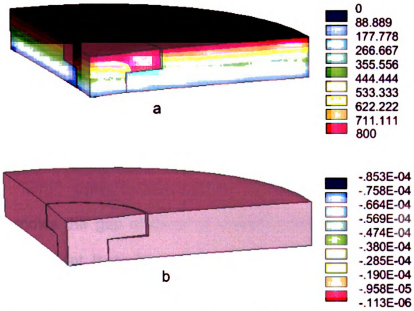

Figure 20. The modified geometry under the 100-750°C temperature gradient (a) temperature distribution (b) gap distance between the ZrW_2O_8 core and RCC skin

The problem with the geometry shown in Figure 20 is that the bottom horizontal part of the upper cylinder always stays in contact with the RCC, making it difficult for the coolant gas to be channeled through the core and out to the exterior surface. Therefore, a slightly different geometry was considered. In this new geometry, the top part was tapered down resulting in a frustum of a cone with a top radius of 15mm and a bottom radius of 7.5mm. The bottom part remained cylindrical with a radius of 7.5mm.

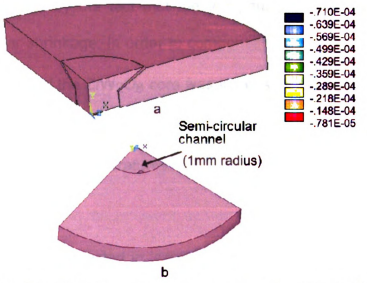

Figure 21. The tapered core geometry under the 100-750°C temperature gradient (a) Gap distance (b) bottom view of the core showing the semi-circular channel that provides larger flow area for the coolant gas

Figure 21 shows the gap distance of modified structure under the 100-750°C temperature gradient. It can be clearly seen that the tapered geometry provides a better and shorter route for the coolant gas. However, small channels should be incorporated into the cylindrical bottom half of the core in order to achieve a higher surface area for continuous flow for the coolant gas. Semi-circular shaped

channels starting from the bottom surface and extending half way up through the core has been simulated. These semi-circular channels had a 1mm radius. There were a total of 4 channels in the core geometry (one channel in the quarter-geometry). The incorporation of the thin channels does not have a significant effect on the gap distance.

It can be seen in Figure 21 that the design with tapered top portion does not provide a gap distance (71 μm) as large as the one with the cylindrical top (85.3 μm). This is caused by the fact that the top portion has a larger dimension, yielding a smaller shrinkage. In order to compensate for this issue, the radius of the bottom cylinder of the ZrW_2O_8 core was increased. This increases the taper angle, resulting in a larger dimension of the core; thus, provides more shrinkage at the top portion at high temperatures.

Several larger radii were tested in order to investigate the relationship between gap distance and the radius of the bottom cylinder, as shown in Figure 22. It can be clearly seen that the gap distance increases with an increase in the bottom radius until 12mm is reached. For the radii larger than 12mm, the gap converges to 94.2μm. Therefore, it proves that changing the bottom radius is an appropriate way to alter the gap distance.

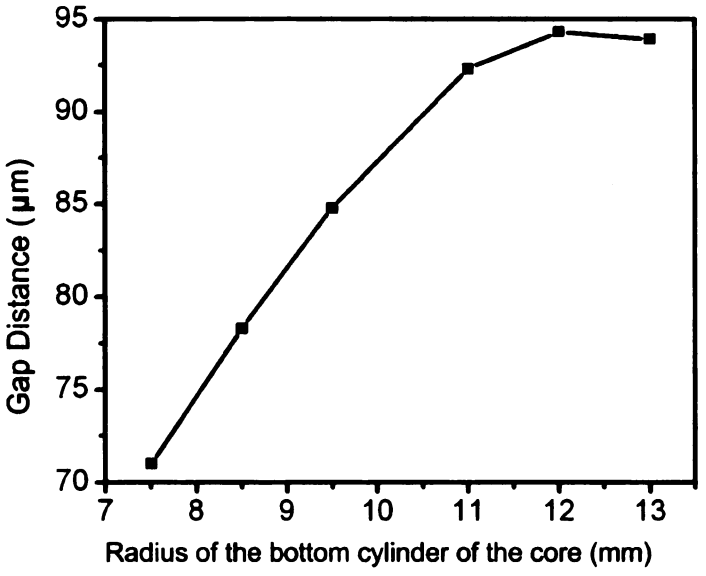

Figure 22. The relationship between the gap distance and the bottom cylinder radius or the core

In order to get the optimal gap distance, the final modified design for the ZrW_2O_8 core had a radius of 12mm for the bottom cylindrical portion. The top radius was kept at 15mm. This final design is shown in Figure 23. Figure 24(a) shows the temperature distribution in the structure for this final design at working condition. Figures 24(b) and 24(c) show the gap distance and maximum principal stress contours at working conditions, respectively. This final design results in a maximum gap distance of 90μm at the working condition. There is a slight decrease from 94.2μm is caused by rounding off the corners and edges which could create stress concentration in the structure. Figure 24(d) shows the maximum principal stress in the structure at room temperature. The maximum calculated stress of 127MPa does not exceed the tensile strength of RCC skin in any directions.

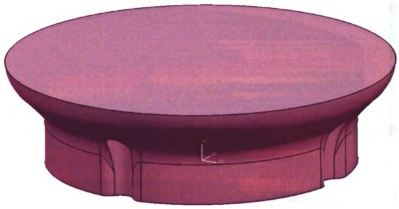

Figure 23. Final geometry for the ZrW_2O_8 core

One problem with this final ZrW_2O_8 core design is that it has a very complex geometry. It was determined that it will be very difficult to manufacture using only powder processing methods. It would require additional finishing operations, which would result in higher costs and may result in a damaged final part. Alternative designs had to be considered in order to make the fabrication less intricate.

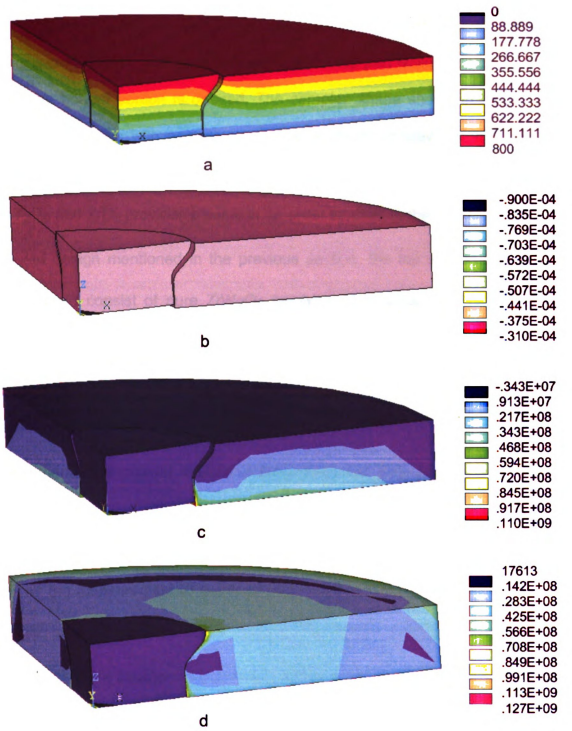

Figure 24. The FEA results for the final ZrW_2O_8 core design a) temperature distribution at working condition (in degrees Celcius) b) gap distance at working condition and c) max principal stress at working condition d) max principal stress at room temperature

2.4.7. Alternative Design for the NTE core

For the core design, a large gap opening at the top part while maintaining a tight fit at the bottom portion is desired. The complex shape shown in Figure 23 is difficult to achieve with powder processing methods. However, considering the gradient temperature characteristic, a cylinder-shaped FGM core containing ZrW_2O_8 and ZrO_2 provides a solution. In order to achieve the similar effect of the tapered design mentioned in the previous section, the top section of the FGM core should consist of pure ZrW_2O_8 because of its large negative CTE. The bottom section should have the appropriate volume ratio of ZrW_2O_8 and ZrO_2 to achieve zero CTE.

Experimentally, a powder mixture of ZrO_2+WO_3 and ZrO_2 powder was stacked, compacted, and sintered in the processing steps commonly used to fabricate multi-layer materials. The observation of the cross-sectional microstructures as well as the measurement of the radial thermal expansion provided the evidence that the sintered samples are continuous FGM made of ZrW_2O_8 and ZrO_2. The continuous FGM structure is due to the diffusion and sublimation of WO_3 as well as the reaction between WO_3 and ZrO_2 during sintering. Varying the soaking time, component of each layer, or the mass/thickness ratio among layers affects the final microstructures and axial CTE distribution [37]. The important property of

this kind of FGM is the continuous variation in the radial thermal expansion from negative to positive. This finding provided the experimental support for the FEA modeling.

In FEA, it is difficult to model a part with continuous property change. Therefore, the modeling of the FGM core was simplified by creating separate layers with different properties and attaching them together in ANSYS. Initially, a 5-layer cylindrical FGM core with a 15mm radius at room temperature was simulated. Each layer had a uniform thickness and linear thermal expansion coefficient throughout the core. The properties as well as the volume ratios of ZrO_2 and ZrW_2O_8 of each layer are shown in Tables 5 and 6. The values are taken from the report of Sun et al [38]. The first layer represents the bottom layer, and the fifth layer represents the top layer.

Table 5. Various parameters for the FGM core

Layer #	ZrW_2O_8/ZrO_2 Volume Ratio	Thermal Conductivity* (W/m/K)	Young's Modulus (GPa)
1	52:48	1.4531	2.24 ± 0.08
2	64:36	1.2099	2.71 ± 0.08
3	76:24	1.1346	3.18 ± 0.10
4	88:12	1.0696	3.65 ± 0.13
5	100:00	0.9672	4.12 ± 0.13

* Calculated by Mori-Tanaka Method [39]

Table 6. CTE values for the FGM core at several temperatures

Layer #	CTE ($10^{-6}K^{-1}$)				
	100°C	150°C	300°C	500°C	800°C
1	-2.25	-7.41	-0.76	-0.76	-0.76
2	-3.83	-9.68	-2.51	-2.91	-2.91
3	-5.4	-11.95	-4.1	-5.03	-5.03
4	-6.98	-14.22	-5.7	-7.3	-7.3
5	-8.56	-16.49	-7.3	-7.3	-7.3

The rest of the finite element modeling was carried out in the same fashion explained in the previous section. Same temperature gradient and boundary conditions were applied to the structure with the new core made of FGM. The results show that the use of FGM core provides a larger gap distance at the top surface (97.7μm) while the bottom part of the core remains in contact with the RCC skin at low temperatures. The maximum stress at contact at room temperature is 5.66MPa, which is significantly smaller compared to the maximum stress created with the tapered ZrW_2O_8 core design. This proves that FGM core is a suitable design alternative to the pure ZrW_2O_8 core. These results are shown in Figure 25.

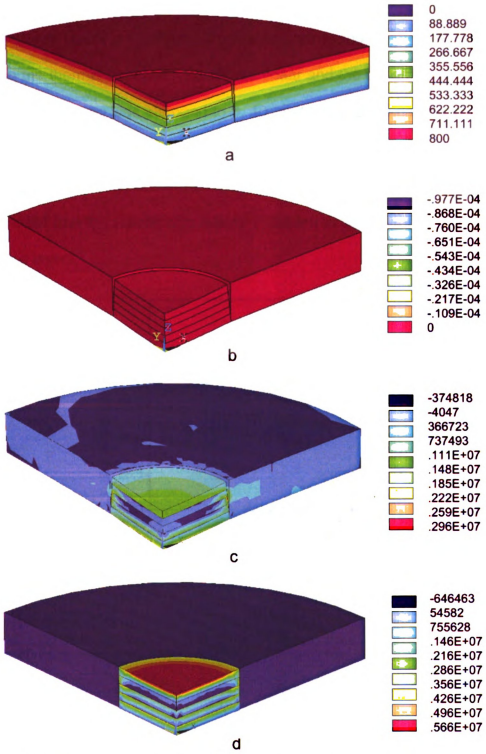

Figure 25. FEA results for the 5-layer uniform FGM core a) temperature distribution at working condition b) gap distance at working condition c) max principal stress at working condition d) max principal stress at room temperature

The effect of increasing the number of layers of the FGM core was studied. When the number of layers is increased, the core becomes more like continuous FGM. Keeping the thermal expansion coefficient linear and the uniform layer-thickness, the number of layers was changed to 8, 10, and 12, and the gap distances were recorded. The results are shown in Figure 26. It can be seen that increasing the number of layers does not have a significant effect on the gap distance. Thus, it is concluded that the results with 5-layer FGM are similar to those with the FGM with more layers.

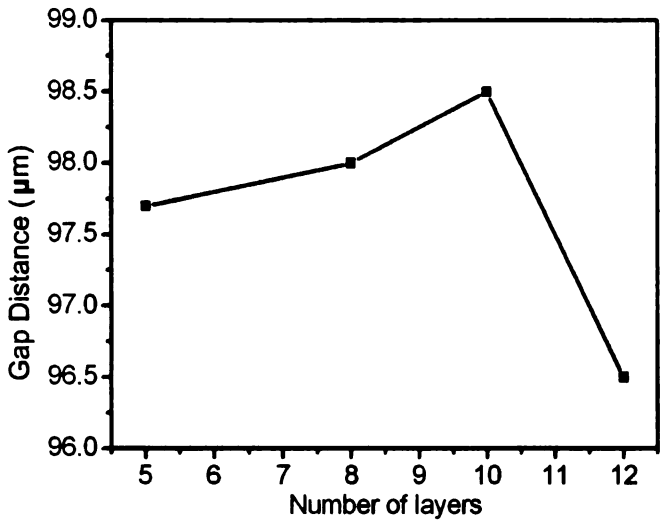

Figure 26. The relationship between the gap distance and number of layers of the FGM core

Additional FEA was performed in order to determine if the gap distance of 97.7μm can be increased. Several different FGM configurations were considered, where the thickness of each layer varied within the geometry. These configurations as well as the corresponding gap distances and stresses can be seen in Table 7.

Table 7. Different FGM configurations for the Perspirable Skin core and their corresponding gap distances and maximum stresses

FGM Configuration	Layer Thickness (mm)*				
	Layer 1	Layer 2	Layer 3	Layer 4	Layer 5
1	3	2	1	1	1
2	4	1	1	1	1
3	3	1	1	1	2
FGM Configuration	**Gap distance (μm)**		**Maximum Stress (Mpa)**		
1	104		3.68		
2	105		1.80		
3	102		2.90		

* Layer 1- top layer, Layer 5-bottom layer

The results show that having a thicker portion of pure ZrW_2O_8 at the top surface while having a linear increase in CTE in the following layers gives a larger gap opening compared to the FGM core with uniform layer-thickness. Since the former contains more ZrW_2O_8, the result is as expected. It must also be noted that the bottom layer of configuration 3 is twice as thick as the bottom layers of the other two designs. This causes a larger portion of the FGM core to stay in contact with the RCC skin providing a more secure fit.

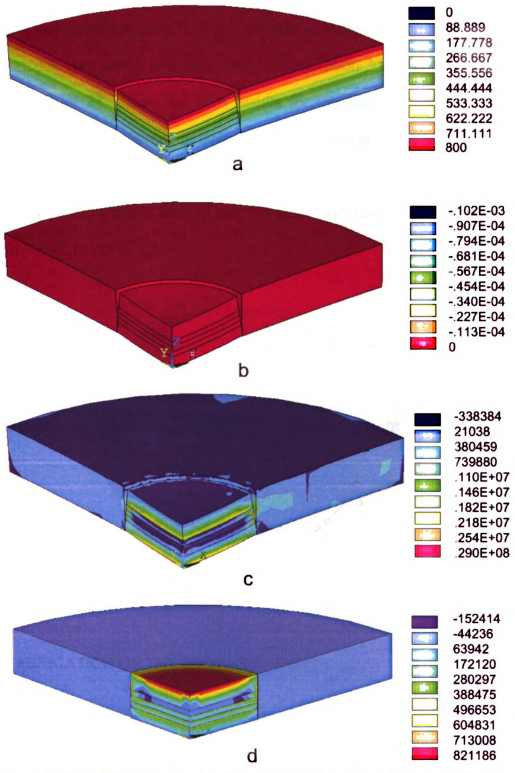

Figure 27. The FEA results for the final FGM core design a) temperature distribution at working condition b) gap distance at working condition c) max principal stress at working condition d) max principal stress at room temperature

Even though configurations 1 and 2 provide a slightly larger gap opening, the difference is very small; and, thus, FGM configuration 3 was chosen as the best design. Figure 27 shows the FEA results for the gap opening and maximum principal stress at different conditions for this design. This FGM design also needs channels at the bottom portion for the coolant gas to be passed through since this portion stays in contact with the RCC skin at all times. The final design is also shown in Figure 28.

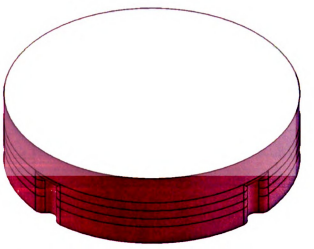

Figure 28. Final geometry for the FGM core with semi-circular channels for the coolant gas to exit

2.5. FABRICATION OF THE FINAL FGM CORE

In order to fabricate similar FGM of the best design experimentally, two WO_3+ ZrO_2 powder mixtures were made. In one powder, the mass ratio of WO_3 and

ZrO_2 is m_{WO3}: m_{ZrO2} =1:0.266 (Powder A), and it is m_{WO3}: m_{ZrO2} =1:0.38 for the other powder (Powder B). Powder A produces pure ZrW_2O_8 after sintering and Powder B produces a composite of ZrW_2O_8 and ZrO_2 with 0 CTE [26]. 1.3g Powder A and 1.7g Powder B were measured and stacked together. After compaction and sintering by the same sintering process for pure ZrW_2O_8 [26], a continuous ZrW_2O_8+ ZrO_2 FGM was made. The height of the sintered sample is 7.7mm. The axial CTE of the sample is shown Figure 29, which is very close to the FEA requirement.

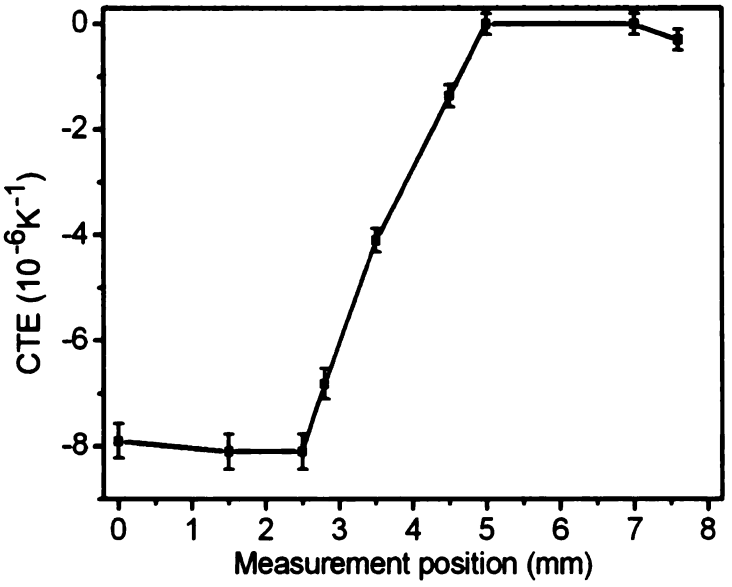

Figure 29. Measured CTE of the best FGM core design

CHAPTER 3

EFFECTS OF POWDER METALLURGY STEPS ON FINAL PROPERTIES OF GREEN BODIES

3.1. INTRODUCTION

As explained in the previous chapters, the best method for fabricating the core of the Perspirable Skin is powder metallurgy. Since the gap distance at both working and assembly conditions is quite small, it is essential to obtain final parts with net-shape and high dimensional accuracy. Large variations in the final dimensions will result in non-uniform gap openings. Additional finishing operations after the fabrication increases costs and may produce defects in the final part [40]. Therefore, it is important to minimize such variations in the powder metallurgy steps. For this reason, the influence of fabrication steps on the shape and density of the final parts must be investigated.

The three main steps of powder metallurgy (mixing, compaction and sintering) explained in Section 1.4 are strongly related to each other. Each step highly influences the subsequent step(s). The initial powder characteristics, such as average particle size [41-44], particle shape [45], particle size distribution [42-44, 46, 47] and specific surface area [42] achieved during powder mixing, influence the compaction and sintering capability. The compaction pressure [43, 48] and the die wall friction [49] of the compaction step can affect the final shape of green compacts as variations in the density distributions can exist in the compact [16,

49]. In this study, the effect of powder mixing on the compaction capabilities of alumina (Al_2O_3) powders as well as the dimension and density variations in the green bodies after the compaction step are investigated. The choice of alumina is due to the fact that it is one of the most commonly studied ceramic powders. It is also inexpensive to test, making it the most attractive material for this study.

3.2. EFFECTS OF POWDER MIXING ON THE COMPACTION CAPABILITIES OF CERAMIC POWDERS

3.2.1. Materials and Experimental Procedure

In this study, several different powder mixtures were produced by mixing any two of four alumina powders. The powders used were TMDAR (Taimei Chemical CO., LTD., Japan), CR-15, CR-6, and GE-1 (Baikowski Ind. Corp., USA). All four types of alumina powders were high-purity, undoped powders with submicron/micron particle sizes. Several properties of these powders are shown in Table 8. CR-15, CR-6, and GE-1 are all produced by the same manufacturer and have nearly identical chemical components. However, they differ in particle size distributions and mean particle sizes, resulting in different compaction characteristics. The reason for choosing TMDAR powder is because it is physically and chemically treated. Its particle size distribution has a very narrow non-lognormal range which results in a sintered product with very low porosity. These two features of TMDAR powder gives rise to its high compaction and sintering capabilities.

Table 8. Properties of the ceramic powders used in the experiments

Material	Powder	Smallest particle size (μm)	Largest particle size (μm)	Mean particle size (μm)	Mean pore size (μm)
Alumina	TMDAR	0.1	0.33	0.17	0.09
	CR-15	0.17	1.15	0.41	0.18
	CR-6	0.23	1.72	0.6	0.27
	GE-1	3.5	23.9	9.76	0.24

Material	Powder	Chemical analysis (ppm)						Bulk density (g/m^2)
		Na	K	Fe	Ca	Si	Mg	
Alumina	TMDAR	4	2	5	3	3	1	0.9
	CR-15	12	15	3	2	21	<1	0.45
	CR-6	13	22	2	3	14	<1	0.6
	GE-1	12	15	5	2	42	<1	0.45

The particle size distribution for each powder was measured in a water solution by the Malvern Mastersizer Micro (Malvern Instruments, England). The results are very close to the manufacturer's report and are shown in Figure 30. It can be seen that the size distributions of CR-15, CR-6 and GE-1 are nearly lognormal.

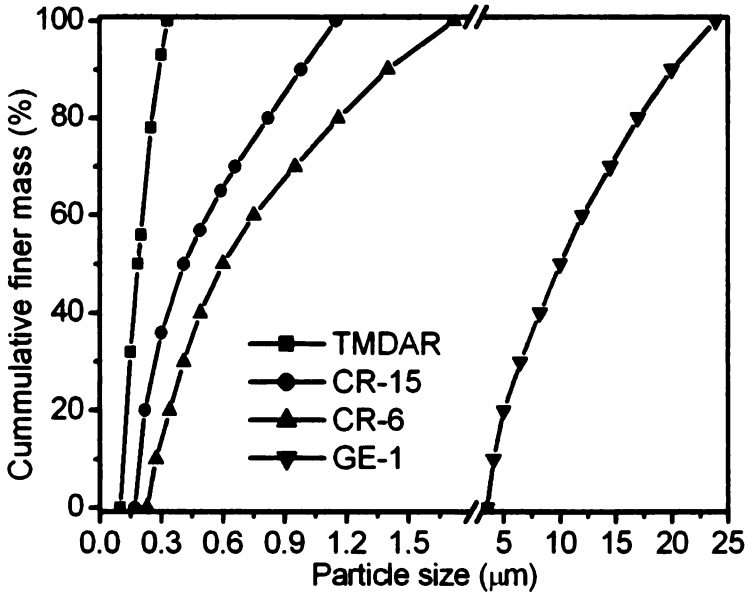

Figure 30. Particle size distributions of the powders used in the experiments

The powders were mixed using the Speed Mixer DAC 150 (FlackTek, Inc., USA) for 3 minutes (1 minute for each cycle and totally 3 cycles) at the angular velocity of 1700 rad/s. A total of six powder mixture systems were produced by mixing all possible two-powder combinations of the four alumina powders with different mass ratios. These mixture systems were: TMDAR+CR-15, TMDAR+CR-6, TMDAR+GE-1, CR-15+CR-6, CR-15+GE-1, and CR-6+GE-1. In addition to four unmixed powders, each system contained nine powder mixtures, in which the proportions of one powder in the mixtures range between 10% and 90% in 10% increments. Therefore, a total of 54 powder mixtures were investigated.

Six grams of each powder mixture was measured by Adventurer AR 2140 (Ohaus Corp. USA) with a 0.0001g resolution; and then poured into a single-action die made of 1144 Stress Proof steel. The inner diameter of the die (D_i) was 22.19mm. Before pouring the powders into the die, the die wall was lubricated with graphite powder (Panef Corp., USA). The top surface of the powder was flattened and then the top punch was inserted into the die until it contacted the powder (refer to Figure 4). The compaction load was applied on the top punch by MTS Insight 300 (MTS Systems Corp., USA). First, a pre-load of 0.5MPa was applied at 5mm/min to set an initial state. This step is necessary in order to measure the compact characteristics accurately before starting the main compaction process. After applying the pre-load, the initial height of each sample, h_i, was measured using a Marathon electronic digital caliper with a 0.02mm resolution and a 150mm measurement range. This was done by measuring the

total height of the two punches and the pre-loaded compact inside the die, then subtracting the height of the two punches. Since the diameter of each compact is equal to the inner diameter of the die (D_i), the initial relative density, (R_i) can be calculated by the following equation:

$$R_i = \frac{\rho_i}{\rho_f} = \frac{m}{\frac{3.975}{4}\pi D_i^2 h_i} \tag{5}$$

where m, V, *and* ρ stand for mass, volume, and density, respectively. The subscripts *i* and *f* stand for the initial and theoretical fully values. The theoretical fully-density of alumina was taken as 3.975g/cm^3.

After calculating the initial relative density, the die set with the pre-loaded compact was placed back in the load frame. It was compacted to 80MPa at a speed of 10mm/min. The stress resolution of the MTS was 0.013MPa. During the compaction, only the top punch moved and the bottom one was stationary. The compressive forces applied on the top (F_t) and bottom punches (F_b) as well as the displacement of the top punch (Z_t) were recorded continuously as a function of time by the load sensors.

The heights of the final green samples ranged from 7.05mm to 9.1mm depending on the powder mixture. Their diameters were 22.19mm, resulting in height/diameter ratios between 0.3 and 0.4. Due to the low height/diameter ratio,

the force transmitted force to the bottom punch and the applied force on the top punch were almost identical in the compaction. The discrepancy between the two recorded forces was less than 0.2%. The masses of the green samples were measured again after compaction. An expected mass change always existed due to the attachment of powders to the die wall and the punches as well as the powder loss during the transport. However, this change was less than 0.4% and was neglected. Several green samples were coated with lacquer and then their volumes were measured in water by Archimedes' principle. Those values were then compared to the corresponding volumes calculated by the final sample heights (h_f) and diameter (D_i). The discrepancies between the two groups of values were less than 1.1%. Therefore, only the calculated volumes are reported in this study.

3.2.2. Results & Discussion

3.2.2.1. Relative Density vs. Stress Relationship

The sample height at any time t (h_t) during the compaction can be calculated using the recorded displacement of the top punch (Z_t) and either the initial compact height (h_i) or initial compact height (h_f) using equations (6) and (7). Using each equation, h_t was calculated to check for consistency and the results obtained from both equations were identical.

$$h_t = h_i - Z_t \tag{6}$$

$$h_t = h_f + Z_t \tag{7}$$

Using h_t, the relative density at any given time (R_t) can now be calculated in by the following equation (8). The corresponding stress (σ_t) can be obtained by dividing the recorded load, F_t, by the cross sectional area of the punch as shown in equation (9).

$$R_t = \frac{\rho_t}{\rho_f} = \frac{m}{\frac{3.975}{4}\pi D_i^2 h_t} \tag{8}$$

$$\sigma_t = \frac{F_t}{\frac{1}{4}\pi D_i^2} \tag{9}$$

Relative density was plotted as a function of stress for each powder mixture system. Figures 31(a) and 31(b) show the plots for TMDAR+CR-15 and CR-6+GE-1 mixtures systems, respectively. Only six different mass ratios are shown in these figures for clarity.

It is obvious from Figure 31 that the relative density increases when the compaction load/stress increases. It can also be seen that two different powder mixture groups show different range of relative densities for the same compaction stress. This difference can be directly related to the compaction capabilities of these powder mixtures. A higher relative density shows better compaction capability. It can also be concluded from Figure 31 that the relationship between

the powder proportions remains similar, even though the overall relative density increases with increasing compaction loads. Thus, this shows that the compaction capability highly depends on the starting powder combination. Additionally, the initial relative densities obtained from the starting powders can be used to quantify and compare the compaction capability of each powder mixture.

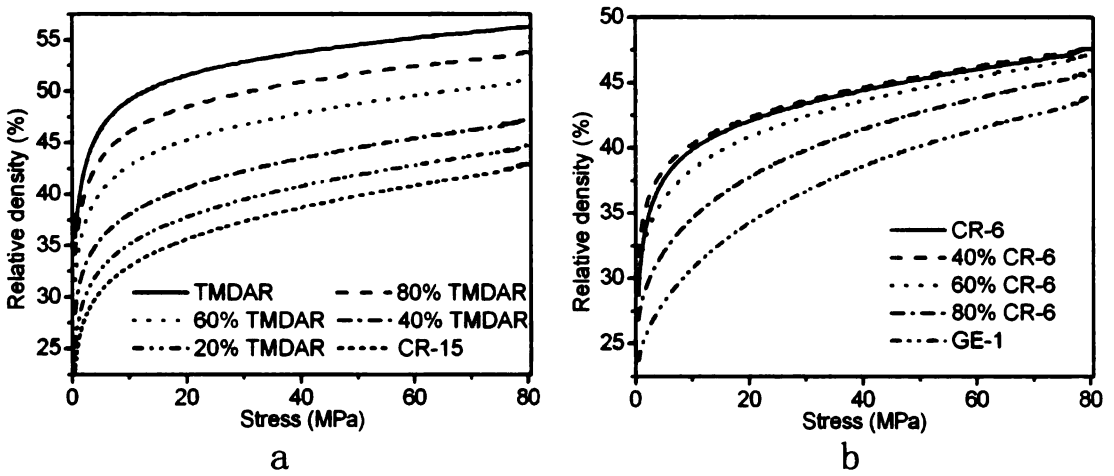

Figure 31. Relative density as a function of stress for two different alumina powder mixture groups at various mass ratios (a) TMDAR+CR-15 group (b) CR-6+GE-1 group

Figure 32 shows the relationship between the initial relative density and the powder proportion for all six of the powder mixture groups. In the each of the powder mixture groups, one of the powders is referred to as the "fine" powder and the other one is referred to as the "course" powder depending on their average particle sizes shown in Table 8. For each of the curves in Figure 32, the mass ratios increase from left to right for the coarse powder, and from right to left for the fine powder.

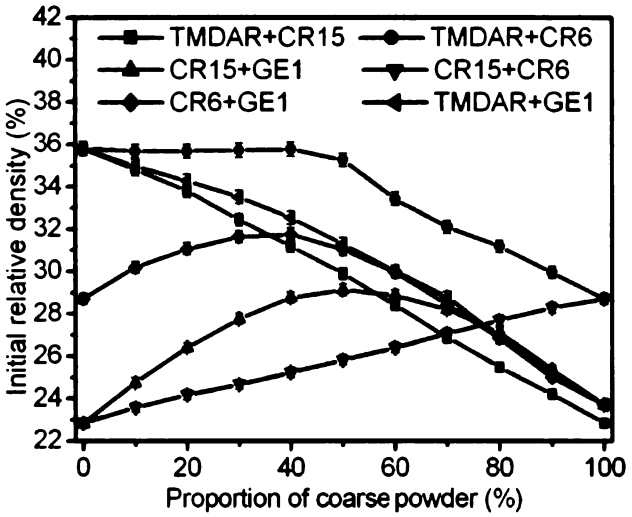

Figure 32. Initial relative density as a function of proportion of the course powder for all six alumina powder mixture groups

Figure 32 shows that there are two different kinds of relationships between the initial relative density and the proportion of the course powder. TMDAR+CR-15 and CR-15+CR-6 groups show a linear relationship, where the maximum relative density corresponds to 100% of one of the powders. TMDAR+CR-6, CR-15+GE-1, and CR-6+GE-1 mixture groups show a nearly parabolic relationship. The proportions of coarse powder in the powder mixture that obtained the maximum relative density are between 40% and 60%. Westman [41] and McGeary [50] reported a similar parabolic relationship for sand and metal balls; however, they found the proportion of the coarse powder that had the maximum relative density to be 30%. Finally, for the TMDAR+GE-1 powder group, the maximum relative density was found to be at 100% TMDAR.

3.2.2.2. Relative Density vs. Strain Relationship

The axial true strain at any given time during the compaction process (ε_t) for ceramic powders can be calculated using equation (10) [16, 51]. Using this relationship, relative density was plotted as a function of strain for the TMDAR+CR-15 and CR-6+GE-1 powder mixture groups. These plots can be seen in Figures 33(a) and 33(b).

$$\bar{\varepsilon}_t = \left| \ln\left(\frac{h_t}{h_i}\right) \right| \tag{10}$$

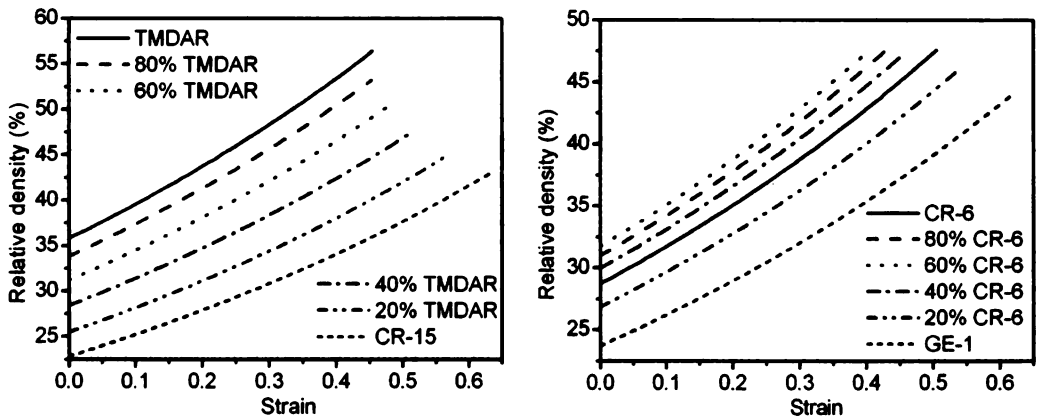

Figure 33. Relative density as a function of axial true strain for (a) TMDAR+CR-15 group and (b) CR-6+GE-1 group

The relationship between relative density and true axial strain can be obtained by finding the equations of the trend lines from the plots using Microsoft Excel 2003. This was carried out for all six powder mixture groups, and it was determined that the relationship is exponential as shown in equation (11):

$$R_t = Ke^{\bar{\varepsilon}t} \tag{11}$$

where K is a constant that varies for each powder mixture group as well as different mass ratios of each powder. It has the same units as density (g/cm^3). It can be seen that powders with a higher K value will have a higher relative density meaning that they have better compaction capability. Table 9 shows the values for K for the TMDAR+CR-15 mixture group at all mass ratios. It was also determined that the values shown on this table correspond to the initial relative density values from Figure 32. This means that the physical meaning of the constant K is actually the initial relative density of the powder mixture. This conclusion can also be verified by combining equations (5), (8) and (10). The final equation is given in equation (12).

$$R_t = R_i e^{\bar{\varepsilon} t} \tag{12}$$

Table 9. Constant K for TMDAR+CR-1 mixture group for all mass ratios

CR-15	0%	10%	20%	30%	40%	50%	60%	70%	80%	90%	100%
K (g/cm^3)	1.423	1.384	1.34	1.3	1.24	1.189	1.13	1.069	1.013	0.962	0.91

It can be concluded that when comparing compaction capabilities of different powder mixtures either using the relative density vs. stress curves or relative density vs. strain curves, the initial relative density is the key parameter that must be considered. The difference in compaction capabilities can simply be compared by using the relationship shown in Figure 32. It must also be noted that the initial relative density is dependent on the pre-load. If the pre-load is decreased, so will the initial relative density. However, the relationship between the strain and initial relative density as well as the order of the compaction capabilities of the different

powder mixtures will remain the same.

3.3. DENSITY VARIATIONS IN GREEN COMPACTS

Green samples may contain two kinds of inhomogeneities, caused by the several operation steps in ceramic powder processing: density distributions as the variation of the internal form and dimensional variability in the external shape of the compact [40, 51-53]. Shape changes that take place during the sintering step are controlled to a large extent by the density distributions within the green compact. A non-uniform density distribution usually results in variations in the net dimensional change from low density to high density areas in the compact. In worst cases, this might cause cracking in the sample due to the stress fields induced by the local variation of shrinkage ratio [51].

Aydin et al. [16, 51] studied the measurement and prediction of the density variations in die-pressed green compacts. In order to detect densification experimentally, they used lead balls as tracers. However, in this method, the lead balls are placed at several positions at a certain distance apart from each other, rather than in a continuous way. In order to overcome this disadvantage, our group used several layers of colored ceramic powder to understand the powder flow, which can indicate the density variations in the green compacts.

3.3.1. Experimental Procedure

Two different types of alumina powders (CR-15 and TMDAR) were dyed using a red-colored water-based stamp ink (2000 plus, COSCO, Germany). The colored powders were then put into a furnace (Carbolite-HTF1700, UK) for four hours at 70^{o}C to dry out. The remaining solid powders were then poured into 12mm diameter alumina mixing media in order to break the solids into smaller particles. The bottles were kept on a jar mill (U.S. Stoneware 64AVM, USA) for 48 hours, and then were sifted to get colored powder with particle size less than 0.3mm.

As discussed in Section 3.1, powder mixing has a significant effect on the compaction capability. If the colored powders have different compaction capabilities than the pure powders, they would alter the density distribution of the green compacts. In order to test the compaction capabilities of the colored powders, they were compacted to 0.5MPa and their initial relative densities were obtained using the methods mentioned in Section 3.1. These values were then compared to the initial density values of pure CR-15 and TMDAR. The colored powder that has the same compaction capability as the pure powder is used as indicator for the experiments.

In order to study the density distribution inside a green body, the height to diameter ratio should at least be around 1. If the height is too short, then the density range will be small making it difficult to identify the high and low density

regions. In this study, the height/diameter ratio was kept between 1.1 and 1.2. A uniaxial compaction method was used in a similar fashion explained in Section 3.1.1. The inner diameter of the die was 19.05mm.

In the experiments, the thickness of each colored powder layer was uniform and equal to around 1/15 of the main powder layers, which had uniform layer thickness as well. Based on the desired height/diameter ratio of the green compact, the mass required for each layer was calculated. The mass for each main powder layer varied between 1.2g and 2g and the mass for the each colored powder layer varied between 0.1g and 0.2g depending on different powders. The use of different mass for different powders is due to the variation in compaction capabilities.

First, the die wall was lubricated with graphite powder (Panef Corp., USA). Then, the first layer of powder, which was always the main powder, was poured into the die. The powder was flattened, and then the top punch, which was also lubricated with graphite powder, was inserted into the die until it touched the powder. After this, a pre-loading stress of 0.5MPa was applied to the powder in order to compact the first layer to a firm enough state. The die set was then removed from the MTS (MTS Insight 300, MTS Systems Corp., USA) and the thickness of the pre-loaded layer was measured. This was done by subtracting the height of the two punches from the total height when the compact is inside the die. The top punch was then carefully removed out of the die and the second

layer (colored powder) was poured in. Following the same steps as the first layer, the colored layer was pre-loaded to a stress of 0.5MPa. This procedure was repeated until all of the layers were pre-loaded. Finally, the layered sample was compacted to 80MPa.

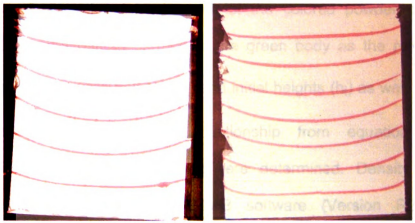

a b

Figure 34. Middle sections of the layered powder compacts (a) CR-15 sample (b) TMDAR sample

The compacted green samples were ejected from the die. They were polished on the lateral surface until the middle axis was reached in order to observe the curves created by the colored powder layers, which are indicators of the densification behavior of the main powder. Each sample was then placed on the sample holder and images of their middle sections were captured using a dissection microscope (Wild M5A, Wild Heerbrugg Ltd, Switzerland) with an attached camera. Figures 34(a) and 34(b) show the images for the CR-15 and TMDAR samples respectively. The bottom side shown in the figures is also the side that contacts the bottom punch during compaction.

3.3.2. Experimental Results & Discussion

The images were analyzed using ImageJ (U.S. National Institutes of Health, USA) software which allows the user to calculate actual distances on the images. The heights of several points on each of the colored powder curves were measured using the bottom surface of the green body as the reference line. Then, using the measured heights (h_t) and initial heights (h_i) as well as the initial relative density-true axial strain relationship from equation (12), the corresponding final relative densities were determined. Density distribution contours were created using MATLAB software (Version R2007b, The MathWorks, Inc., USA). Figures 35(a) and 35(b) shows the contour plots of TMDAR and CR-15 powders, respectively. Due to the symmetry in the density distribution, only half section of the powder was plotted. Thus, the 0 position corresponds to the center axis of the cylindrical shape. It is obvious from these figures that the high-density regions are on the central axis, and the highest density is observed in the bottom central region. The top central regions as well as the bottom edges are the low-density regions. These results are similar to the reports of Aydin et al. [16, 51], and Train [53]. Another point that should be noted is that the density distribution range is different for TMDAR and CR-15. This is due to the fact that TMDAR powder has a better compaction capability, which results in larger overall densities in its density distribution graph.

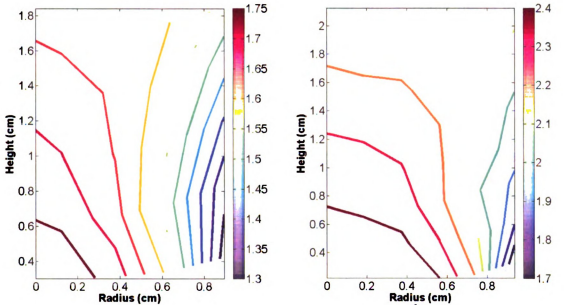

Figure 35. Contour plots of the density distributions in green compacts (a) CR-15 sample (b) TMDAR sample

3.3.3. Finite Element Analysis

Finite element analysis was carried out using ABAQUS (Version 6.6, Dassault Systèmes Simulia Corp., USA) in a similar fashion explained in Aydin et al.'s report [16]. The modified Drucker-Prager / Cap Plasticity model was employed in the modeling of the compaction and ejection process. This plasticity model is available in the library of the software. A 2-dimensional axisymmetric model of the powder bed was created. The die wall as well as the upper and lower punches were modeled as rigid surfaces. A 4-node bilinear axisymmetric quadrilateral element type was used from the axisymmetric stress family. A tangential contact behavior with a friction coefficient of 0.2 was implemented for the interaction property between the die wall and the powder. Figure 36 shows a

schematic of the model with the mesh. The upper punch could move in the z-direction, where the die wall and bottom punch were fixed in all directions.

The compaction process was modeled in three steps similar to Aydin et al.'s method [16]. First the compaction load was applied on the powder by the upper punch. After the powder was compacted to 80MPa, the upper punch was removed which allows the compact to relax in the z-direction while it is still in the die. Finally, ejection was simulated by removing the bottom punch and the die wall.

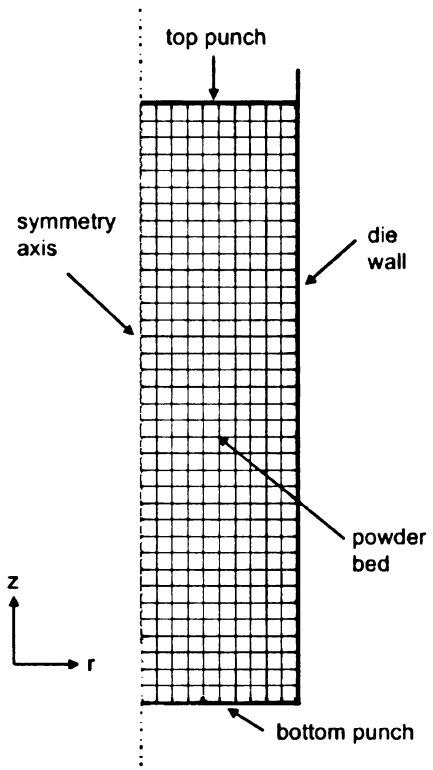

Figure 36. Finite element model for powder compaction

There are several parameters required as user input for the modified Drucker-Prager / Cap Plasticity model in ABAQUS. These parameters include bulk modulus (K), shear modulus (G), Young's modulus (E), Poisson's ratio (v), angle of internal friction (β), material cohesion (d), cap shape parameter (R), and transition surface parameter (α) [15, 54]. In the current study, we used a similar technique used by Chen et al [54] for determining the bulk, shear, and elastic moduli as well as Possion's ratio. The transition surface parameter and the cap shape parameter were also taken from the report of Aydin et al. [16] as 0.03 and 0.558 respectively. The angle of internal friction (β) was varied from 27 to 33.6 degrees and the corresponding material cohesion (d) values were calculated. These two parameters are paired together and the relationship is based on Aydin et al.'s method [16]. The paired numbers are related to the Young's modulus and other mechanical properties as well as the yield surface function. The choice of the minimum angle of 27 degrees is from findings of Zeuch et al. [55].

Contour plots of relative density were created for all three steps of the compaction process. The relative density was a user defined variable which was computed using a subroutine. Figures 37, 38, and 39 show the relative density variations of the CR-15 powder for angle of internal friction values (β) of 27, 28, and 29 degrees, respectively. The results were quite similar for all β values when the compact is in the die before the removal of the top punch. At this step, the density distributions agree with Aydin et al.'s report. The density range however

is different, due to the fact that the Young's Modulus value of our powder was much lower because no binder was used in the experiments.

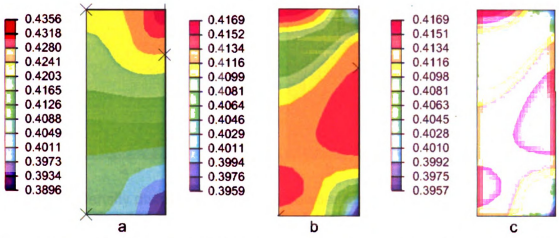

Figure 37. Density distribution of CR-15 powder for $\beta = 27^{o}$ and d = 3.60MPa (a) After compaction (b) after the removal of top punch (c) after the removal of bottom punch and die wall (relative density shown)

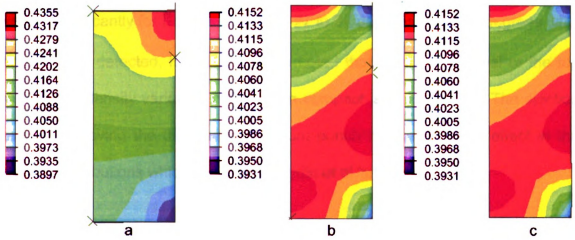

Figure 38. Density distribution of CR-15 powder for $\beta = 28^{o}$ and d = 3.24MPa (a) After compaction (b) after the removal of top punch (c) after the removal of bottom punch and die wall (relative density shown)

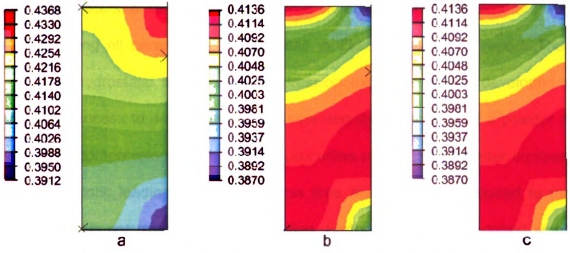

Figure 39. Density distribution of CR-15 powder for $\beta = 29^{o}$ and d = 2.88MPa (a) After compaction (b) after the removal of top punch (c) after the removal of bottom punch and die wall (relative density shown)

The main change in the relative density distributions for different β values was observed when the top punch was removed. The high- and low- density regions varied significantly for β values between 27 to 29 degrees. After 29 degrees, little change was detected. It should also be noted that after the removal of the top punch, the density variation in the green compact is close to final. The ejection step of removing the die wall and bottom punch has close to no effect in the density distributions which is similar to Aydin et al.'s findings [16].

The high-density region at the top central section and the low-density region at the bottom right corner are in good agreement with the findings from the experiments. However, the high- and low-density regions in middle section did not exactly agree. This is due to the fact that most of the parameters for the modified Drucker-Prager / cap model are unique material properties. With so

many parameters, there are numerous possible combinations. An accurate way of determining all parameters is discussed in Zeuch et al.'s [55] report. They performed hydrostatic and triaxial compression experiments and developed a two-stage process to determine the pressure-density relationship of a powder in hydrostatic compression, as well as the properties of the same powder compact under deviatoric loading. However, at this time the equipment required to run similar tests is not available in our facilities. Further analysis is required when necessary devices are obtained.

3.4. DIMENSIONAL VARIATIONS IN GREEN COMPACTS

One of the most important requirements in the production of ceramic products is to attain overall dimensions that are within specified tolerances. However, as mentioned earlier, due to the series of steps in powder metallurgy, green compacts may exhibit dimensional variability in their external shapes [40, 51-53]. This means that the geometry of the external surface of the ceramic green body will not be exactly the same as the terminal geometry of die cavity after the green ejection. Important questions remain regarding the evolution of the external shape of the green compacts during the compaction process [40].

3.4.1. Experimental Procedure

In this study, the external shapes of the various green bodies from Section 3.1 were measured using a Veelo-DEKTAK 6M Stylus Profiler with a resolution of 0.5nm (Fraunhofer, LLC, Coating Technology Division, USA). In order to support the samples, a special base was designed and fabricated. A simple schematic of the setup is shown in Figure 40. The green sample was placed on the base and the probe of the profiler contacted the external surface of the green sample. A 3mg force was applied on the probe and then the probe moved from one edge to the other edge to measure the external surface profile. After one measurement, the sample was rotated by 90 degrees on the base and another measurement was performed. A total of four measurements were taken for each sample.

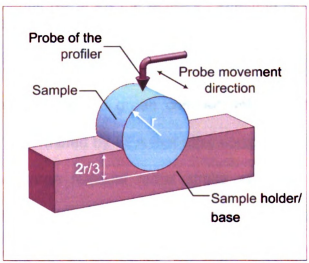

Figure 40. Simple schematic of the setup for external shape measurements

3.4.2. Experimental Results & Discussion

The variation in the diameter along the thickness of the sample was calculated by taking the average of the four measurements for each of the samples. The diameter variation of the CR-15 sample is shown in Figure 41. It was determined that all of the samples exhibited a lateral shape similar to a barrel.

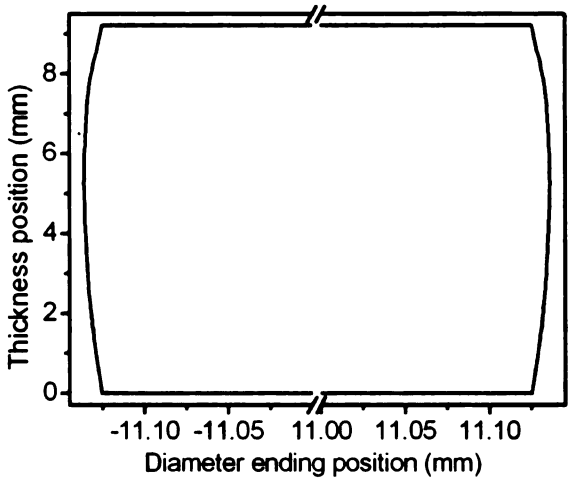

Figure 41. Experimental result for the diameter variation along the thickness of the CR-15 green sample

Aydin et al. [40] reported that a green compact takes its final form after the ejection step. They determined by FEA that after compaction, the green samples inside the die have large residual radial stress at about the middle of the compact, and small redial residual stress on the top and bottom surface. After the ejection of the green sample, the compact is freed in the radial direction. Therefore, the high stress regions relax radically and form regions with larger diameter regions in the final greens. This results in a final shape similar to a barrel.

From Figure 32, it is obvious that CR-15 powder has the lowest compaction capability. From the measurements, it was determined that the difference between the largest and the smallest diameter for the CR-15 sample is 23.21μm. Pure TMDAR powder, which is has best compaction capability, exhibited a difference of 6.3μm between the largest and smallest diameter. For all the other samples, this diameter variation is between 6.3μm and 23.21μm. Figure 42 shows the diameter difference for the TMDAR+CR-15 and CR-15+GE-1 mixture groups. When this figure is compared to Figure 32, it can be determined that the powder mixtures that have better compaction capability exhibit smaller diameter difference. Since such powders are denser; hence shorter in height, the residual stress variation while inside the die will also be smaller. This will result in less barreling for the powders with better compaction capability. It must also be noted that the curves in Figure 32 exhibit almost a mirror image of their corresponding curves in Figure 42. This means that the dimensional variations of the green samples can be estimated by their compaction capabilities.

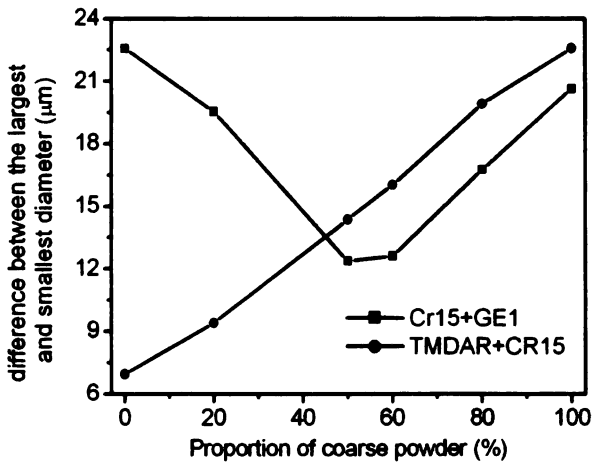

Figure 42. Difference between the largest and smallest diameter as a function of proportion of the course powder

3.4.3. Finite Element Analysis

A preliminary finite element analysis was carried out in a similar fashion explained in Section 3.3.3. The powder bed had a diameter of 22.19mm. Several simulations were performed with different β-d pairs. In all cases, the green compact showed a lateral shape similar to a barrel after ejection, agreeing with the experimental results. The final dimensions were calculated by obtaining the coordinates of all the external surface nodes of the deformed shape. These values were then input into Mircocal Origin software to create a plot similar to Figure 41. Figure 43 shows the FEA results for the CR-15 powder with an angle of internal friction of (β) 33 degrees and a material cohesion (d) of 1.34MPa.

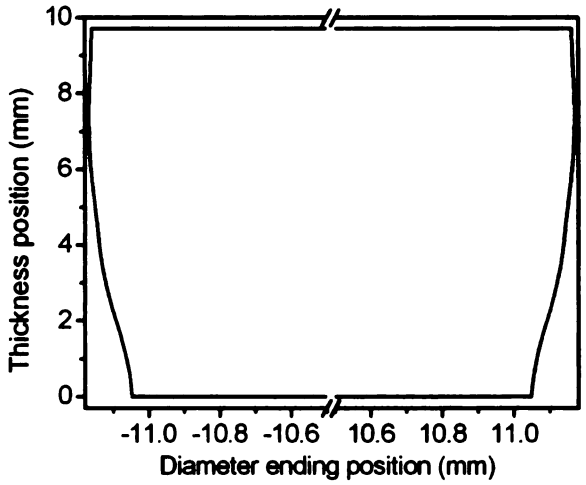

Figure 43. The diameter variation along the thickness of the CR-15 green sample obtained by FEA ($\beta = 33^{o}$, d=1.34MPa)

It is obvious from Figure 3.14 that the location of maximum diameter was close to the experimental results. However, the green sample from FEA exhibited a thinner bottom portion than the experimental sample. This is due to the same

reason explained in Section 3.3.3. At this time, it is not possible to obtain an exact match between the experimental and FEA results without determining all of the parameters needed for the constitutive model used in the finite element modeling. The next step is to determine the required parameters experimentally by running hydrostatic and triaxial compression tests. FEA should then be performed again in order to verify the experimental results.

CHAPTER 4

DISCUSSION AND CONCLUSIONS

4.1. DISCUSSION AND CONCLUSIONS

Perspirable skin, an autonomous and reusable self-cooling system, was designed for externally heated surfaces of space vehicles, utilizing the negative thermal expansion property of ZrW_2O_8. The best RCC fiber arrangement for the Perspirable Skin was determined to be 3D woven orthogonal by finite element modeling. Its high tensile strength in both longitudinal and transverse directions, as well as its thermal expansion capabilities allow for a safe and efficient application.

FEA was also used to determine the best design for the core geometry. Due to the temperature gradient that the structure experiences, the design with a larger radius at the top surface and a smaller radius at the bottom surface guarantees the contact of the two materials while providing a large gap at working condition. Tapering the top portion of the core into a frustum of a cone was necessary in order to allow for an efficient flow path for the coolant gas between the ZrW_2O_8 core and the RCC skin; however this design did not provide a large enough gap opening at the top surface. Increasing the bottom radius of the ZrW_2O_8 core compensated for this problem. Additionally, thin semi-circular shaped channels

were incorporated into the cylindrical bottom half of the core to allow continuous flow of coolant gas at high temperatures.

Initially, the tapered ZrW_2O_8 core design was chosen as the best design; however it was determined that this design is difficult to manufacture by powder metallurgy methods. Switching to a cylinder-shaped FGM for the core provided ease in manufacturing, larger gap distance, and lower stresses in the overall structure. The top surface of the FGM core consisted of pure ZrW_2O_8 due its large negative CTE and the bottom portion had the appropriate volume ratio of ZrW_2O_8 and ZrO_2 that gave a linear increase in CTE all the way up to zero. The final FGM design was successfully fabricated using powder metallurgy methods.

Since the gap opening both at working and assembly conditions is in the micro scale, it is very important to fabricate the core with a net-shape and high dimensional accuracy. Large variations in dimensions will result in non-uniform gap openings. However, due to the series of operation steps in powder metallurgy, the final parts may exhibit several structural inhomogeneities, such as density variations and dimensional discrepancies [40, 51-53].

The three main steps of powder metallurgy (mixing, compaction and sintering) are strongly related to each other. Each step highly influences the following step(s). Therefore, influences of fabrication steps on several properties of the

final parts were investigated. In the experiments, several different alumina powders were used. The choice of alumina is due to the fact that it is one of the most commonly studied ceramic powders. It is also inexpensive to test, which made it the most appealing material for this study.

First, the effect of powder mixing on the compaction capabilities of ceramic powders was studied. This was done by mixing several two-powder combinations of four alumina powders at various mass ratios and examining their green densities as a function of stress and true axial strain. It was concluded that powder mixing has a strong influence on the compaction capabilities of ceramic powders. It was also determined that the initial relative density of the powder mixture is the key property that can be used to predict compaction capability.

The internal form of structural inhomogeneities in the green bodies is the density variations [16]. Next, two different alumina powders were tested using layers of colored powder in the main powder in order to detect density distributions. The layered powder was compacted to 80MPa. After the ejection, the green body was polished on the lateral surface until the middle axis was reached. It was observed that the colored powder layers showed curved lines, rather than straight, indicating that the density distribution is non-uniform. This trend can be observed in the fabrication steps of ZrW_2O_8-ZrO_2 FGM samples as well. When a layer of ZrO_2 and another layer of ZrO_2 + WO_3 powder mixtures are compacted to produce FGM containing ZrW_2O_8 and ZrO_2, a boundary is formed between the

two layers due to the uneven powder distribution after compaction. It is easy to see the curved boundary because of the color difference in the powders used (Figure 44(a)). Fortunately, due to the diffusion and sublimation of WO_3 as well as the chemical reaction between the two powders, this non-uniformity in the density distribution will begin to decrease [56]. If the soak duration is long enough, a sample with uniform density can be obtained, as shown in Figure 44(b), which was sintered at 1180°C for 16 hours.

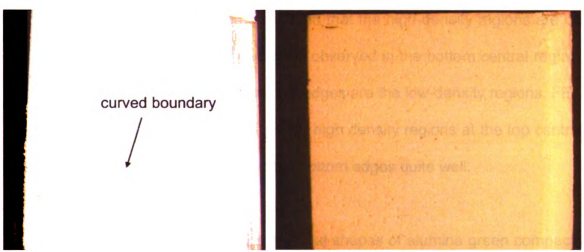

Figure 44. The middle section of the FGM sample after different fabrication steps (a) after compaction (b) after sintering

Shape changes that take place during the sintering step are controlled to a large extent by the density distributions within the green compact. A non-uniform density distribution usually results in variations in the net dimensional change from low density to high density areas in the compact. In worst cases, this might cause cracking in the sample due to the stress fields induced by the local variation of shrinkage ratio [51].

It is essential to study density variations in green bodies, in order to predict and minimize dimensional variations and cracks in the sintered samples. The density distributions of the layered compacts mentioned in Section 3.3 were analyzed both experimentally and numerically. Experimentally, the final heights (h_f) of several points on each of the colored layers were measured. Then, using the initial relative density-true axial strain relationship from equation (10) the corresponding relative densities were determined. Contour plots of density distributions were created. It was concluded that the high-density regions are on the central axis, and the highest density is observed in the bottom central region. Top central regions as well as the bottom edges are the low-density regions. FEA predicted the density range, as well as the high density regions at the top central region and the low-density regions at the bottom edges quite well.

Finally, dimensional variations in the external shapes of alumina green compacts from the compaction capability experiments were analyzed, both experimentally and numerically. It was determined that geometry of the external surface of the ceramic green body was not exactly the same as the geometry of die cavity after the green ejection; rather it exhibited a barrel shape. This finding is similar to the report of Aydin et al. [40] who explained the cause of such shape as a result of the relaxation of the high stress regions in the radial direction after the ejection step. It was also concluded that the powder mixtures that had the higher compaction capability, had a lower difference in the maximum and minimum

diameter values. This shows that the compaction capability is a good indicator of the final external shape of green bodies.

4.2. RECOMMANDATIONS FOR FUTURE WORK

One difficulty with the Perspirable Skin design is the incorporation of holes into the RCC TPS. Drilling into the RCC structure will cut through the fibers, causing a significant decrease of strength. In order to compensate for this, incorporation of the holes must be completed during fabrication of the RCC TPS. Another possible solution is the use of a 3D woven orthogonal RCC with a large enough fiber bundle to accommodate the diameter of ZrW_2O_8 core within each bundle in order to avoid damaging the carbon fibers in the structure. The assembly of the core and the skin parts is the next step in the design process.

When comparing the experimental and numerical results of the density distributions and final external shapes of green compacts, the findings were overall in good agreement. However, some discrepancies were detected between the FEA and experimental results. This is due to the fact that most of the parameters used in the constitutive model in FEA are unique material properties. With so many parameters, there are numerous possible combinations. An accurate way of experimentally determining all the required parameters is a combination of hydrostatic and triaxial compression tests [55]. However, at this time the equipment required to run similar tests is not available

in our facilities and further analysis is required when necessary devices are obtained.

BIBLIOGRAPHY

[1] Angelo J. A., 1999, *The dictionary of space technology*, New York, NY: Facts on File, pp. 211-25.

[2] NASA Facts, 2006, "Orbiter Thermal Protection System", FS-2004-09-014-KSC (Rev. 2006), pp. 1-6.

[3] Cleland G. G., Iannetti F., 1989, "Thermal protection system of the space shuttle", *NASA contractor report*: NASA CR-4227, pp.1-17

[4] Richard S., 1980, "Orbiter Protective Tiles Assume Structural Role", *Aviat Week & Spa Tech.*, Feb.25, pp. 22-24.

[5] Savage G., 1993, *Carbon-carbon composites,* New York, NY, Chapman & Hall, pp. 37-80 & pp. 322-350.

[6] NASA facts, 2006, "Reinforced Carbon-Carbon (RCC) panels", FS-2004-01-001-KSC (Rev. 2006), pp. 1-2.

[7] Mary T. A., Evans J. S. O., Vogt T., Sleight A. W., 1996, "Negative thermal expansion from 0.3 to 1050 Kelvin in ZrW_2O_8", *Science.*, **272**(5258), pp. 90-92.

[8] Yang P. D., Zhao D. Y., Margolese D. I., Chmelka B. F., Stucky G. D., 1998, "Generalized Syntheses of large-pore mesoporous metal oxides with semicrystalline frameworks", *Nature.*, **396**(6707), pp. 152-155

[9] Kalpakjian S., Schmid S. R., 2008, *Manufacturing Processes for Engineering Materials*, Upper Saddle River, NJ, Pearson Education, Inc., pp. 669-726.

[10] Kieback B., Neubrand A., Riedel H., 2003, "Processing techniques for functionally graded materials", *Mater Sci Eng A.*, **362**, p. 81.

[11] German R.M., 1994, *Powder metallurgy science*, 2nd ed., Metal powder industries federation, Princeton, pp. 15-24, 210-221, 241-262.

[12] Miyamoto Y., Kaysser W.A., Rabin B.H., Kawasaki A., Ford R.G., 1999, *Functionally Graded Materials: Design, Processing, and Applications,* Springer, pp. 1-5

[13] Reddy J. N., 2006, *An Introduction to the Finite Element Method,* New York, NY: McGraw-Hill, pp. 1-26

[14] Gallagher R. H., 1975, *Finite Element Analysis Fundamentals*, Englewood Cliffs, NJ, Prentice-Hall, Inc., pp.3-5.

[15] Dassault Systèmes Simulia Corp. (formerly Abaqus, Inc.), 2007, *ABAQUS Theory Manual*, Version 6.6, Section 4.4.4-1

[16] Aydin I., Briscoe B. J., Sanliturk K. Y., 1996, "The internal form of compacted ceramic components: a comparison of a finite element modeling with experiment", *Powder Technology.*, **89**, pp. 239-54

[17] Drucker D. C., Prager W., 1952, "Soil mechanics and plastic analysis of limit design", *Q. Appl. Math.*, **10** pp.157-65

[18] Drucker D. C., Gibson R. E., Henkel D. J., 1957, "Soil mechanics and work-hardening theories of plasticity", *Am. Soc. Civil. Eng. Trans.*, **122**, pp.338-46

[19] Sleight A. W., 1995, "Thermal contraction", *Endeavor.*, **19**(2), pp. 64-68.

[20] Evans J.S.O., Mary T. A., Sleight A. W., 1998, "Negative thermal expansion materials", *Physica B.*, **241-243**, pp. 311-16.

[21] Sleight A. W., 1998, "Compounds that contract on heating", *J inorg. Chem.*, **37**, pp. 2854-60.

[22] Mary T. A., Evans J. S. O, Vogt T, Sleight A. W., 1996, "Negative thermal expansion from 0.3 to 1050 Kelvin in ZrW_2O_8", *Science.*, **272**(5258), pp. 90-92.

[23] Evans J. S. O., Mary T. A, Vogt T., Subramanian M. A, Sleight A. W. "Negative thermal expansion in ZrW_2O_8 and HfW_2O_8", 1996, *Chem Mater* **8**(12), pp.2809-23.

[24] Closmann C., Sleight A. W., Haygarth J. C., 1998, "Low-temperature synthesis of ZrW_2O_8 and Mo-Substituted ZrW_2O_8", *J Solid State Chem* **139**(2), pp.424-26.

[25] Korthuis V., Khosrovani N., Sleight A. W., Robers N., Dupree R., Warren W. W. Jr., 1995, "Negative thermal expansion and phase transitions in the $ZrV_{2-x}P_xO_7$ series", *Chem Mater*, **7** pp. 412-17.

[26] Sun L., Sneller A., Kwon P., 2008, "ZrW_2O_8-Containing composite with near-zero coefficient of thermal expansion fabricated by various methods: Comparison and optimization", *Compos. Sci. Technol.*, **68**(15-16), pp. 3425-30

[27] Chen J. -C., Huang G. -C., Hu C., Weng J. –P., 2003, "Synthesis of negative-thermal-expansion ZrW_2O_8 substrates", *Scripta. Mater.*, **49**, pp.261-66

[28] Yang X., Cheng X., Yan X., Yang J., Fu T., Qiu J., 2007, "Synthesis of ZrO_2/ZrW_2O_8 composites with low thermal expansion", *Compos. Sci. Technol.*, **67**, pp.1167-71.

[29] Lommens P., De Meyer C., Bruneel E., De Buysser K., Van Driessche I., Hoste S., 2005, "Synthesis and thermal expansion of ZrO_2/ZrW_2O_8 composites", *J. Eur. Ceram. Soc.* **25**(16) pp. 3605-10.

[30] Sheehan J. E., Buesking K. W., Sullivan B. J., 1994, "Carbon-Carbon Composites", *Annu. Rev. Mater. Sci.*, **24**, pp. 19-44.

[31] Tanabe Y., Yasuda E., Kimura S., Iseki T., Maruyama T.,, Yano T., 1991, "Neutron irradiation effects on dimension and mechanical properties of carbon fiber/carbon composite", *Carbon.*, **29**(7), pp. 905-08.

[32] Kennedy C. A., White M. A., 2005, "Unusual thermal conductivity of the negative thermal expansion material, ZrW_2O_8", *Solid. State. Commun.*, **134**(4), pp.271-276.

[33] DryMiotis F. R., Ledbetter H., Betts J. B., Kimura T., Lashley J. C., Migliori A., Ramirez A. P., Kowach G. R., Van Duijn J., 2004, "Monocrystal elastic constants of the negative-thermal-expansion compound Zirconium Tungstate (ZrW_2O_8)", *Phy.s Rev. Lett.*, **93**(2)025502, pp. 1-4.

[34] Kundu P. K., Cohen I.M., 2008, *Fluid Mechanics*, Elsevier p.335

[35] Jacobson N.S., Leonhardt T. A., Curryc D.M., Rappd R.A., 1999, "Oxidative attack of carbon/carbon substrates through coating pinholes", *Carbon.*, **37**, pp. 411–19

[36] Oguz B., Sun L., Kwon P., 2008, "Perspirable Skin: A Multifunctional Material System for Self-Cooling", *Proc. for 1st ASME Conference on Smart Materials, Adaptive Structures and Intelligent Systems,* SMASIS2008-525.

[37] Sun L., Baldauf S., Kwon P., 2008, "Procession of ZrW_2O_8-ZrO_2 continuous Functionally graded materials by co-sintering ZrO_2 and ZrO_2+WO_3 multi-layer compacts", *2008 ASME International*

Manufacturing Science and Engineering Conference Proc., MSEC_ICM&P2008-72368

[38] Sun L., Shi X., Sneller A., Uher C., Kwon P., 2008, "In-situ synthesis and thermal properties of ZrO_2/ZrW_2O_8", *Proc. for the 23rd Annual Technical Conference of ASC*, pp.14-23.

[39] Mori T., Tanaka K., 1973, "Average stress in matrix and average elastic energy of materials with misfitting inclusions", *Acta. Metal.*, **21**(5), p. 571.

[40] Aydin I., Briscoe B., Sanliturk K. Y., 1997 "Dimensional variation of die-pressed ceramic green compacts: comparison of a finite element modeling with experiment", *Eur. Ceram. Soc.*, **17**, pp.1201-12.

[41] Westman A. E. R., Hugill H. R., 1932, "The packing of particles", *J. Am. Ceram. Soc.*, **13**, pp. 767–79.

[42] Lance D., Valdivieso F., Goeuriot P., 2004, "Correlation between densification rate and microstructural evolution for pure alpha alumina", *J. Eur. Ceram. Soc.*, **24**, pp. 2749–61.

[43] Sun L., Sneller A., Kwon P., 2008, "Fabrication of Alumina/Zirconia functionally graded material: from optimization of processing parameters to phenomenological constitutive models", *Mater. Sci. Eng. A*, **488**(1-2), pp. 31-38.

[44] Sun L., Sneller A., Kwon P., 2009, "Powder selection in cosintering multi-layered ceramic functionally graded materials based on the densification kinetics curves", *J Comp Mat.*, **43**(5), pp.469-482.

[45] White H. E., Walton S. F., "Particle packing and particle shape", 1937, *J. Am. Ceram. Soc.*, **20**(5), pp.155-66.

[46] Ting J. -M., Lin R. Y., 1994, "Effect of particle-size distribution on sintering", J. *Mater. Sci.*, **29**(7), pp.1867-72.

[47] Ting J. -M., Lin R. Y., 1995, "Effect of particle size distribution on sintering: Part II Sintering of alumina", *J. Mater. Sci.*, **30**(9), pp.2382-89.

[48] Kim K. T., Choi S. W., Park H.,2000, "Densification behavior of ceramic powder under cold compaction", *J. Eng. Mater. Technol.*, **122**(2), pp.238-44.

[49] Brisco B. J., Rough S. L., 1998, "The effects of wall friction in powder compaction", *Colloids and Surfaces A.*, **137**, pp.103-16.

[50] McGeary R. K., 1961, "Mechanical packing of spherical particles", *J. Am. Ceram. Soc.,* **44**(10), pp. 513-22

[51] Aydin I., Briscoe B., Sanliturk K. Y., 1994, "Density distributions during the compaction of alumina powders: a comparison of a computational perdition with experiment", *Comput. Mat. Sci.*, **3**, pp. 55-68.

[52] Agarwal J. C., 1986, "Process economic and strategies in the advanced ceramics industry., *Adv. Ceram. Mater.*, **1**, pp.332-34

[53] Train D, 1957, "Transmission of forces through a powder mass during the process of pelleting", *Trans. Instn. Chem. Engrs.*, **35**, pp. 258-66.

[54] Chen W.F., Baladi G.Y, 1985, *Soil Plasticity*, New York, NY, Elsevier, pp.79-83

[55] Zeuch D.H., Grazier J. M., Argüello J. G., Ewsuk G. K., 2001, "Mechanical properties and shear failure surfaces for two alumina powders in triaxial compression", *J. Mater. Sci.*, **36**, pp. 2911-24

[56] Kuribayashi K., Yoshimura M., Ohta T., Sata T., 1980, "High-temperature phase relations in the system Y_2O_3-Y_2O_3·WO_3", *J Am Ceram Soc.* **63**(11-12), pp. 644-47.